REVIEW ARTICLE OPEN

Check for updates

A critical review of the recent advances in inclusion-triggered localized corrosion in steel

Pan Liu[1,2], Qin-Hao Zhang[3], Yutaka Watanabe[1], Tetsuo Shoji[1] and Fa-He Cao[3]✉

Localized corrosion triggered by inclusions is prone to metallic material failure. Except for chemical dissolution of some special inclusions, the principle of galvanic coupling is the most acceptable theory to explain the above corrosion damage mechanism over the past decades. Still, controversies continue to present, in particular, mounting recent evidence obtained by advanced technologies emphasizes the limitations of previous entrenched idea and discloses unexpected results. Here, we review relevant recent studies and carefully summarize their similarities and differences to reduce the knowledge gap between inclusion-triggered localized corrosion and material design, whilst the source of typical inclusions is treated and discussed.

npj Materials Degradation (2022)6:81 ; https://doi.org/10.1038/s41529-022-00294-6

INTRODUCTION

Xiu, a Chinese character rhyme corresponding to rust in English, has long been noticed and is interpreted as a colorful garment on the metal surface by the ancients. Although sages used this feature of rust merely as a metaphor to illustrate that fresh metal surface exposed to a natural atmospheric environment tends to be chemically and/or electrochemically eroded and generates multicomponent corrosion products, it was a physical-chemically nontrivial observation that the atoms located at the multiphase interface are favorable to move towards a more stable state and lower energy through a series of physical stacking and/or chemical reactions[1–6].

Beyond its literary meaning, the link between metal corrosion and human beings has lasted for around thousands of years. As an inevitably natural occurring phenomenon, honestly, corrosion extremely increases the failure risk of the metallic materials in service and greatly promotes the staggering size of economic costs, particularly after mankind stepped into the iron age (due to the thermodynamic stability of most iron-based materials is lower than that of copper-based materials). As reported, the wallet paid for corrosion by adding up the costs associated with corrosion-induced upkeep, repair, replacement and other externalities generally accounts for around 1–5% annual gross national product of each country[7]. Nevertheless, the magnitude and seriousness of corrosion-related issues have also been raising awareness of the people since centuries, especially for policy makers in the relevant industries and researchers dedicated to the corrosion field, such that better decisions and excogitations are spurred to enhance competence against corrosion risk[8].

Among various kinds of corrosion forms, localized corrosion as one of the inconspicuous corrosion types has long been a headache for corrosion community around the global. Compared with uniform corrosion, localized corrosion is named for the local centralized corrosion damage on the metal surface resulting from corrosion galvanic cell caused by local electrochemical inhomogeneity, and can be normally divided into six types, namely galvanic corrosion, pitting corrosion, crevice corrosion, intergranular corrosion, selective corrosion and corrosion under the joint influence of stress and corrosion factors[9]. Also, once it starts, the rapid propagation speed will give birth to unanticipated failure ranging from mild to catastrophic. Accordingly, imperceptible destructive localized corrosion is used to be conceivable as a likely culprit for the collapse of most metal-based civilization[10–14].

Despite demanding challenges for detection, longstanding research efforts have fully demonstrated that the observed localized corrosion is, in general, closely related to certain kinds of internal macro-defects in metallic materials (precipitates, second phase, inclusions, etc.) by means of various new ex-situ electron microscopy techniques, such as bright-field and high angle annular dark-field (HAADF) STEM, precession electron diffraction, nano-beam electron diffraction, X-ray energy dispersive spectroscopy as well as some in-situ methods like liquid-cell scanning/transmission electron microscopy, electron energy loss spectroscopy and so forth, as depicted in Fig. 1[15], since it is widely perceived that miniature galvanic cells are prone to be formed in these places due in large part to potential difference between defects and adjacent metal matrix thanks to the heterogeneity in element composition or the discontinuity of surrounding passive film[16–20]. Controversies still exist, though, doubts regarding the applicability of traditional galvanic coupling theory on deciphering localized corrosion triggered by internal defects in metallic materials, particularly the inclusion-induced selective dissolution in steel, was recently raised again by scholars based on some unexpected evidence, which evinces that overwhelmingly used traditional mechanism can sometimes fail in practice and reminds us that our mechanistic understanding for some inherent phenomena is still rudimentary[21–26].

Fortunately, with the aid of modern sophisticated devices with high spatial resolution and combination of computational modeling methods, the knowledge gap is gradually narrowing, which offers an effective shortcut for researchers to track the exact location where selective dissolution occurs and further verify the data acquired from the experimentation. This in turn facilitates an increasingly accessible multi-dimensional understanding of localized corrosion. Besides, considering the ubiquity of steel in infrastructure makes inclusion-triggered localized corrosion a global concern, and the perception for its underlying mechanism remains controversial till now, which has aroused our great interest.

[1]Frontier Research Initiative, NICHe, Tohoku University, Sendai 9808579, Japan. [2]Department of Chemistry, Zhejiang University, Hangzhou 310027, China. [3]School of Materials, Sun Yat-sen University, Shenzhen 518107, China. ✉email: caofh5@mail.sysu.edu.cn

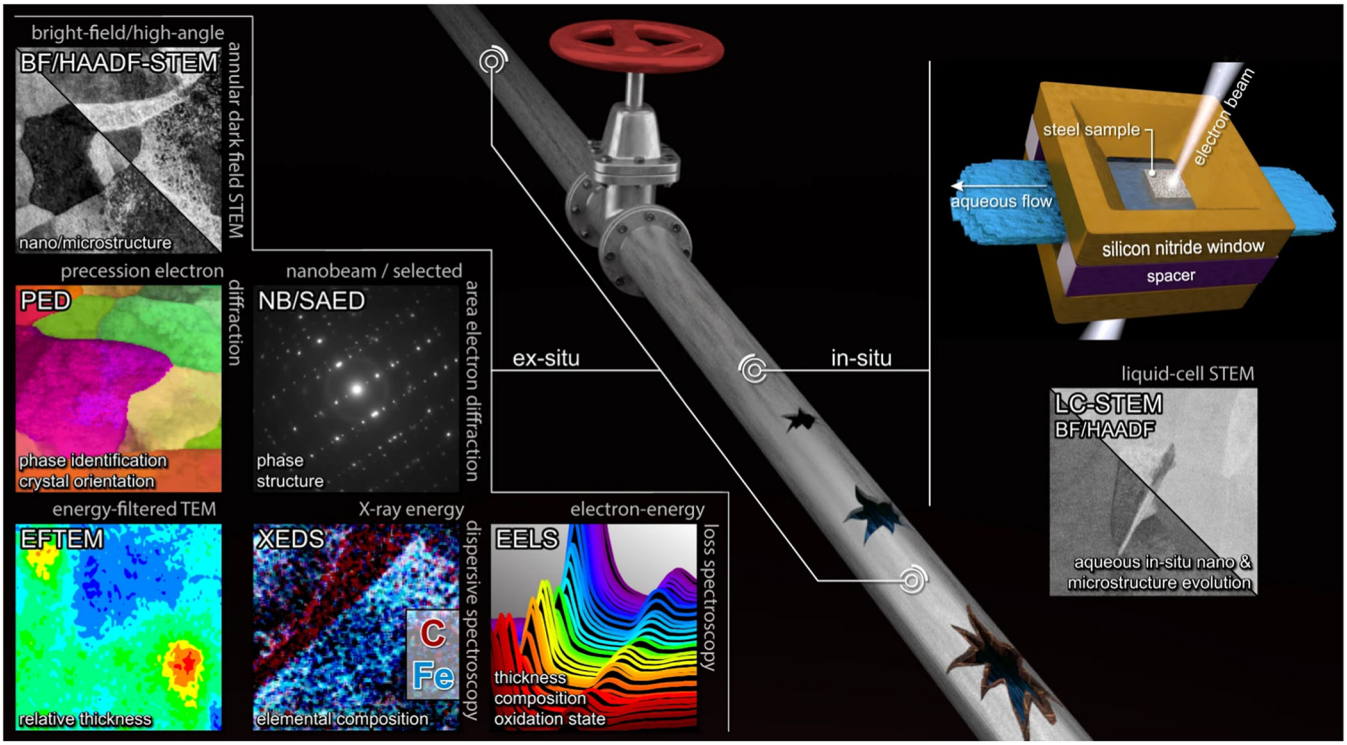

Fig. 1 A representative localized corrosion research workflow. A series of in situ and ex situ new experimental methodologies at the micro-scale and/or nano-scale[15].

Here, how some typical inclusions affect localized corrosion of steel are carefully reviewed by summarizing some fresh landmark works. In addition, the source of some typical inclusions formed in steel is also treated and discussed based on massive studies. Compared with conventional works on similar topic, the major attraction of the current work is to compare and elaborate the similarities and differences in the mechanisms of several typical inclusions-triggered localized corrosion by combining our experience in this field and the novel conclusions of related works in recent years, and thereby point out the contradictions with the entrenched recognition in the past. Certainly, responses to these controversies are not only the testament for the wisdom of ancient sages, but a profound insight into inclusion-induced localized corrosion. Moreover, we expect to give a hand to these who are the beginners in the industry a comprehensive cognition through the present work and provide a practical prospect for the future-related works.

SOURCE OF THE INCLUSIONS IN STEEL

This section is mainly devoted to discussing how some typical inclusions in steel are formed, while the introduction of this plot is beneficial to deepen the appreciating of localized corrosion induced by inclusions in the follow-up. Alternatively, this issue indeed is an old-fashioned theme and has been summarized by a number of previous works[16,27–35]. To the best of our knowledge, though, those summaries are either general or one-sided to some extent. As such, it is necessary to treat and discuss this theme comprehensively one more time with clarity and purpose. In order to make the classification more hierarchical, except for the exogenous inclusions mixed with external impurities in the production process, we are bold to define another inclusions as the following two types in the current work, namely secondary-derived inclusions and nascent inclusions. In addition, the inclusion-triggered localized corrosion will also be described for the above two categories in subsequent sections.

Secondary-derived inclusions

Secondary derived-inclusions mainly refer to a kind of heterogeneous components different from iron (Fe)-based matrix occasioned by artificially adding other elements to remove impurity elements in the process of steel smelting. Among them, non-metallic such as sulfide inclusions and oxide inclusions are the most typical.

Deoxidizing and desulphurizing the steel in an argon-stirred vessel, sometimes in a vacuum degasser is commonly the first refining step in most metallurgical process for steel-making, since trace amounts of impurity elements, such as oxygen (O), nitrogen (N), and sulfur (S) mainly originating from the outside are usually dissolved in molten steel produced in a basic oxygen furnace or electric furnace[36,37]. Yet, these impurity elements are impossible to be completely removed, and tend to form low-melting point eutectic, even employing the modern advanced equipment for control, whilst the formation of these eutectics also shows a potential threat to the properties of steel. As can be seen from a typical phase diagram for the Fe-S-O system illustrated in Fig. 2, the coexistence of elements O and S greatly influences the solid–liquid phase transition temperature of eutectic, especially the temperature for pure Fe-S eutectic is around 1273 K[38]. which easily results in the failure of metallic materials owing to the occurrence of hot shortness in metallurgical industry nowadays.

Considering risk avoidance and some special purpose, an appropriate deal of other elements with a thermodynamic affinity for S and O, such as manganese (Mn), silicon (Si), magnesium (Mg) and aluminum (Al), is always artificially introduced as effective deoxidizers or desulfurizers during smelting to alleviate the negative effects of elements O and S, but diverse undesirable non-metallic secondary derived-inclusions are more or less produced. Meanwhile, a part of secondary derived-inclusions slowly develop by random collision during Brownian motion between each other and/or by the diffusion of constituent elements from bulk molten steel[36]. As a result, non-metallic inclusions with different and separate shapes and sizes but the

same composition are ubiquitous in the steel matrix, while molten steel flows in the solidifying shell (the flow promotes the inclusions to float up to the top slag layer, and produces defects in the cast product by impelling the inclusions to move further down and entrap in the steel during the cooling and solidification procedures).

It has to be admitted that the most of secondary derived-inclusions in steels are commonly considered to be detrimental to their materials properties, particularly increasing the formation odds of internal blisters, slivers, and cracks as well as the chances of localized corrosion due to macro-defects always appear surrounding them occasioned by various coefficient of thermal expansion (the physical properties of typical components possibly used in this work are shown in Table 1[39–45]), and are costly since it is quite difficult to be discovered until after placing in operation, but sometimes the existence of an appropriate amount is conductive for the optimization of materials mechanical properties. Take MnS inclusions as an example, they are always regarded as an indispensable components in free-cutting steel and are always roughly classified into three types, namely (i) spherical shape, (ii) round-bar shape and (iii) dumbbell shape (Fig. 3a–d), based on its morphology[46,47]. Also, its formation mechanism of particles with diverse morphologies is similar to that stated above. Despite this, MnS with different sizes always exhibits its unique good plasticity compared with most other inclusions. Supports from Fig. 3 illustrate that around 85.32% of the spherical inclusions with blue marks and shape factor less than 2 remarkably decreased to 57.31%, whereas the proportion of round-bar and dumbbell inclusions with shape factor more than 2 and respectively marked with red, green, gold, light cyan and orange noticeably rises to 42.69% after rolling process, and this property also enhances MnS inclusions to be extensively used in austenitic stainless steel.

Despite of prominent plasticity, the presence of large-size and non-spherical MnS inclusions is not often expected for most of steels, since the plastic deformation of MnS inclusions during rolling is favorable to result primary cracks propagation at contact

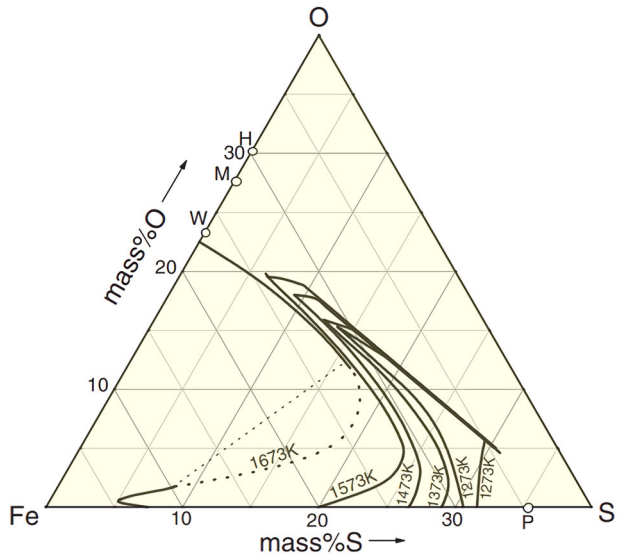

Fig. 2 Phase diagram for the Fe-S-O system. Solid line and dotted line are liquidus and miscibility gap. Point W, point M, point H and point P stand for FeO, Fe_3O_4, Fe_2O_3, and FeS, respectively[38].

Table 1. Physical properties of typical components used in this work[39–45].

Compounds	Thermal expansion coefficient ($\times10^{-6}$/°C)	Electrical volume resistance at 20 °C (Ω cm)	Refs.
MnS	17.4/16.3	-	39
CaS	14.7	$>10^{13}$	40,41
Steel	10.8	1×10^{-5}	42,43
TiN	9.4	27	40,41
Ti_2O	8.4	74	40,41
$MgO{\cdot}Al_2O_3$	8.4	$>10^{15}$	41,42
Al_2O_3	8.2	8×10^{15}	44,45

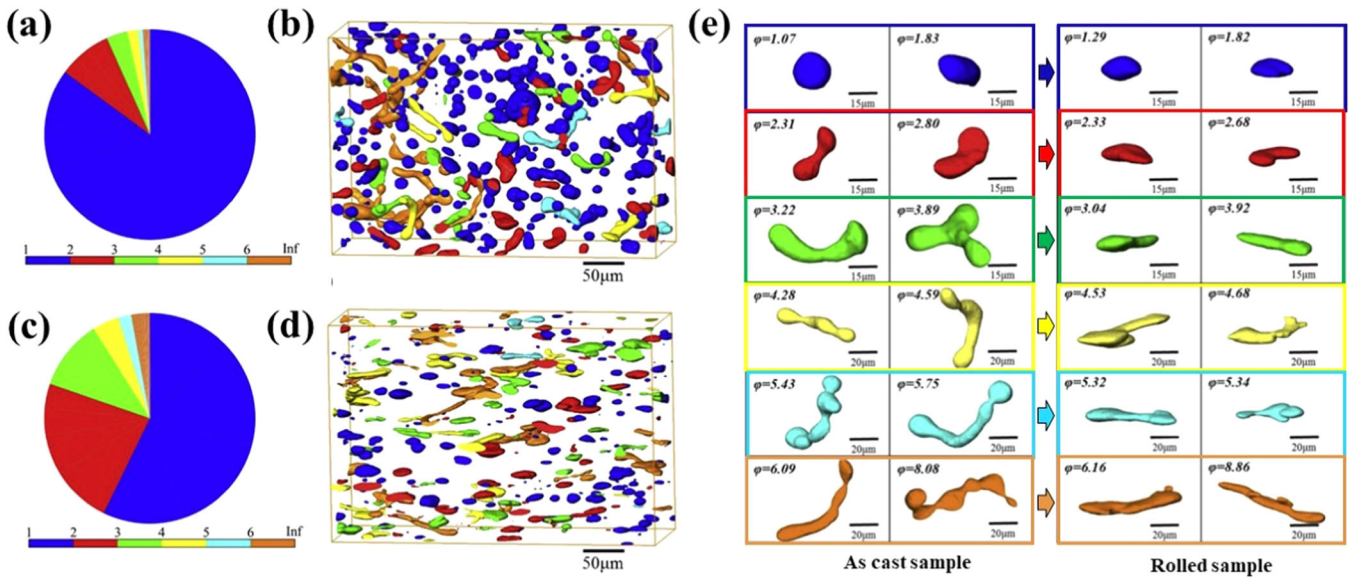

Fig. 3 Comparison of the shape factor distribution of two-types of MnS inclusions. a Statistical and **b** typical spatial distribution of MnS inclusions in as-cast sample. **c** Statistical and **d** spatial distribution of MnS inclusions in samples in the same spatial region after tensile deformation. **e** Typical Morphology of different types of MnS inclusions before and after deformation. Note that inclusion particles in the figures are colored by the individual identification number for the convenience of illustration[47].

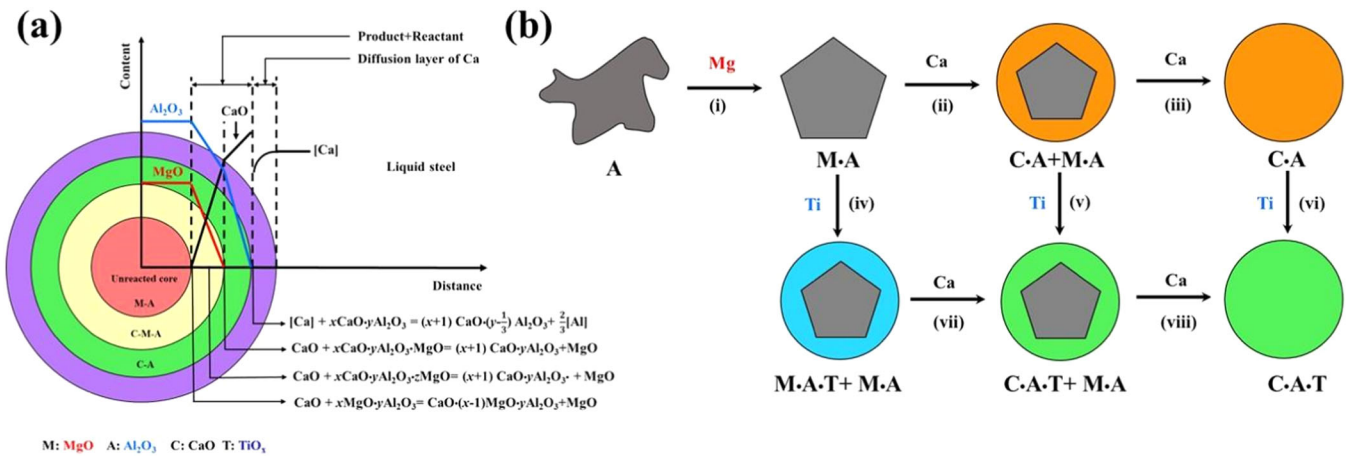

Fig. 4 Schematic diagram of the evolution of MgO-Al_2O_3 system after adding typical elements. a Sketch of evolution of MgO-Al_2O_3 system after adding addictive element Ca and **b** the illustration of modification evolution route of the MgO-Al_2O_3 inclusion in steels with/without element Ti addition[55,56].

sites between inclusions and matrix, and significantly deteriorate the corrosion resistance of steel. As a consequence, a secondary calcium (Ca) modification as another vital step is introduced in the treatment of most steels to decrease the size of secondary derived MnS inclusions and simultaneously reduce the size of possible primary cracks, while the Gibbs free energy of CaS is also the lowest than that of other sulfides at distinct temperature, contributing to the most stable CaS in non-aqueous system[48]. Significantly, Mn element in MnS usually cannot be completely replaced by calcification treatment. It is reported that a layer with (Mn, Ca)-S as main component is formed on the outer surface of MnS inclusions after calcification treatment, effectively precluding the deformation of MnS inclusions and their negative impacts in the rolling process[44,49–51].

Except for MnS inclusions, the secondary Ca modification also shows good efficacy in the modification of other kinds of non-metallic inclusions, particularly a class of tough and hard inclusions. In terms of such inclusions, magnesium–aluminum spinel inclusions with Al_2O_3 and MgO as the main components is a typical example, they are more harmful than soft and deformable MnS inclusions to some extent and are potentially damaging for any part of the production process including rolling, cutting, welding, and so forth.

Abundant conventional achievements finished by laboratory and industrial experimentations have proven that these spinel inclusions enable to be transformed into a liquid calcium aluminate inclusions via Ca additions[44,52–54]. A sketch regarding the evolution of MgO-Al_2O_3 system drawn by Deng et al.[55] was depicted in Fig. 4a, which demonstrates that the main components of the outer edge tend to evolve to CaO-MgO-Al_2O_3 after Ca addition, whilst this transformation gradually changes the shape of the inclusion into a sphere thanks to the melting temperature of CaO-MgO-Al_2O_3 system is relatively lower than that of molten steel. Furthermore, substitution of element Ca for element Mg in inclusions with the diffusion of element Ca leads to the gradient change of MgO to be completely opposite to that of CaO in the same direction, which brings about the gradual formation of calcium aluminate, while it is noteworthy that the whole inclusion will be totally transformed into $xCaO{\cdot}yAl_2O_3$ system as long as the reaction time is long enough (Fig. 4b). Certainly, along with element Ca, there are many other elements with strong affinity and thermal stability with oxygen, such as element titanium (Ti) (Fig. 4b) and various rare earth elements, and are selected in production according to the performance requirements of various products. Although the principle of their modification in terms of MgO-Al_2O_3 system is similar to that of Ca treatment, their solubility is generally less than that of element Ca[56]. Hence, the addition of these elements is not usually for the primary purpose of impurity removal, but mostly for other special requirements. Compared with previously introduced secondary derived-inclusion, this resulting inclusions indirectly generated by adding specific elements for design of functionalized steel are expected to be named as the nascent inclusion in this work, which would be described in detail next.

Nascent inclusions

To achieve special properties, addition of one or several alloying elements during smelting processes is general a customary approach for some steels to realize this purpose. Thanks to strong affinity of some alloying elements, however, a certain proportion of them would be unexpectedly precipitated in the form of inclusions under appropriate conditions by combining with impurity elements. In contrast to the inclusions described in Section 2.1, which are composed of specially added impurity-removing elements, such kinds of inclusions are referred to nascent inclusions here. Inclusions such as TiN formed in Ti-stabilized steel are a typical type of this class.

As one of the Ti-stabilized steels, ultra-pure stainless steel has been extensively applied in automotive exhaust systems owing to its relatively lower purchasing cost and satisfying capacity to withstand high operating temperatures during service[57]. In addition, it is generally believed that element carbon (C) mainly presents in the pearlite and cementite phases, which enhances the cathode activity of the micro-domain and increases the risk of interphase galvanic corrosion in aggressive environments. Interestingly, the addition of Ti, as a ferrite forming element, not only promotes a complete ferritic microstructure during solidification, but precludes the formation of these cathode phases by way of combining element C to form TiC precipitates, which indirectly endows Ti-stabilized steel acceptable corrosion resistance. Dramatically, however, TiN inclusions are favorable to be produced as well due to the relatively strong affinity between elements Ti and N, sometimes Ti-(C, N) inclusions are possibly to be generated (note that TiN is also a by-product of impurity N element sometimes in other kinds of steels). Compared with spherical or elongated MnS, the three-dimensional morphology of TiN inclusions with distinct sizes features obvious faceted cubic shape with sharp edges and angles (Fig. 5a), the two-dimensional computed tomography slices of one target inclusion in *X* direction, *Y* direction and *Z* direction by cross-sections method also suggest that the morphology of TiN has distinct angular characteristics (Fig. 5b)[58]. Meanwhile, it is well known that final form of a particle

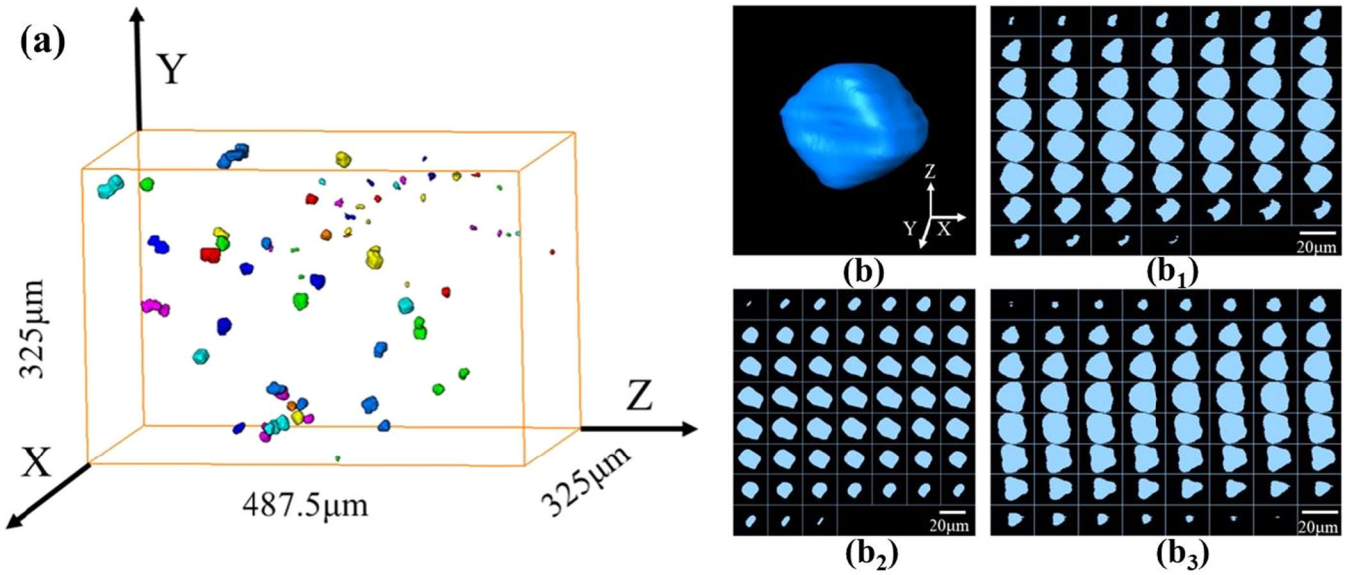

Fig. 5 Three-dimensional spatial distribution and profile morphology of TiN inclusions. a Spatial distribution of TiN inclusions in a space of around 0.051 cm^3 in steel after three-dimensional reconstruction. **b** A typical three-dimensional morphology of a single TiN particle and its corresponding two-dimensional computed tomography slices in $\mathbf{b_1}$ *X* direction, $\mathbf{b_2}$ *Y* direction, and $\mathbf{b_3}$ *Z* direction, respectively[60].

is ordinarily associated with the internal intrinsic lattice structure and the external growth factors, while the former is considered to be beneficial to the equilibrium crystal shape (ECS) with minimum total surface energy[59]. In terms of TiN inclusions, faceted ECS prompts TiN inclusions to be cubic eventually[60].

Nevertheless, great deal of previous experience has proven that the existence of TiN significantly contributes to the refinement of grain, promotion of ferrite laths formation and the improvement of drawability of steel by intensifying the {1 1 1} fiber texture, although it increases the risk of localized corrosion on account of its dissimilar dissolution behavior from matrix[60–64].

INCLUSION-INDUCED LOCALIZED CORROSION

It has been reiterated several times when discussing the source that inclusions acting as a kind of second phase easily give rise to localized corrosion thanks to the different dissolution behavior between inclusions themselves and the metal matrix, and such above inclusions are usually defined as active inclusions.

Honestly, the active and inactive inclusions do not refer to a certain type, since the boundaries of them are vague. Also, most conventional works already identify the chemical and/or electrochemical stability of most non-metallic oxide inclusions is relatively weak compared with sulfide inclusions. Thereby, the latter are used to be regarded as active inclusions by professional personnel. Recently, however, novel evidence highlights that the reactivity for some inclusions is closely related to the content or the distribution of specific components, which once again gives us new insights. For instance, a very recent work of Zhang and Wu[65] reveals that the content changes of $CaO{\cdot}Al_2O_3$ and $CaO{\cdot}2Al_2O_3$ are the key factor for the activity of (Ca, Mg, Al)-O_x-S_y inclusions to trigger the initiation of localized corrosion, when they investigated correlation between active/inactive inclusions and related localized corrosion of EH36 steels, while another distinctive work focusing on $MnCr_2O_4$ nano-octahedron in catalyzing localized corrosion of austenitic stainless steels carried out by Ma and his team[66] also reflects that the reactivity of spinel $MnCr_2O_4$ nano-octahedron with metal terminations in MnS inclusions is much higher than O-terminated ones. Besides, the selective dissolution induced by active inclusion is normally divided into two types, in spite of diverse opinions, the one is traditionally attributed to the thermodynamic instability of inclusions themselves and the other is triggered by the anisotropy between inclusions and matrix.

Thermodynamic instability of inclusions

In terms of thermodynamic instability, CaS is undoubtedly the most classic representative and it is also a sort of typical by-products of the modification of sulfide-type secondary-derived inclusions and/or sometimes the main products for removal of impurity S as mentioned in Section 2.1. Thanks to its negative Gibbs free energy, the presence of water-soluble CaS inclusions in steel, as a consequence, is vulnerable to local preferential dissolution through its chemical dissolution, particularly in aggressive environment[44,48]. The information in Fig. 6 fully highlights this feature.

Although typical secondary electron (S.E.) images of CaS inclusions and associated elements distribution based on the results of energy dispersive spectrometer (EDS) analysis before (Fig. 6a-6a_7) and after (Fig. 6b-6b_7) exposure to 0.1 M NaCl solution at ambient temperature for 1 h were not taken at the same location, a careful comparison of them can demonstrate fully that the CaS inclusions have dissolved in a wide area after immersion, while the adjacent matrix does not show pronounced dissolution different from other locations, which provides an intuitive support for good water solubility of CaS[67]. Moreover, on the basis of the prediction of corrosion performance by the slab models of three low-indexed crystallographic planes (Fig. 6c), it enables to know that the surface energy (E_{surf}) values of Fe in the <1 0 0>, <1 1 0> and <1 1 1> orientations are 2.670 J m^{-2}, 2.511 J m^{-2} and 2.857 J m^{-2}, respectively, whereas this values for CaS particles respectively decrease to 1.671 J m^{-2}, 1.832 J m^{-2} and 2.492 J m^{-2} in three orientations, further sufficiently attesting a higher possibility of electrons in CaS particles escaping from the lattice and a higher risk of corrosion initiation in CaS-contained regions[22]. In addition, the Pourbaix diagram combined with the possible chemical and/or electrochemical reaction formula is ordinarily used by the corrosion community as the criterion for judging the stability of substances under characteristic conditions. As can be seen in Fig. 6d-6d_2, immune zones for CaS inclusions are absent over the entire pH range at 298.15 K in Fe-Ca-S-H_2O system,

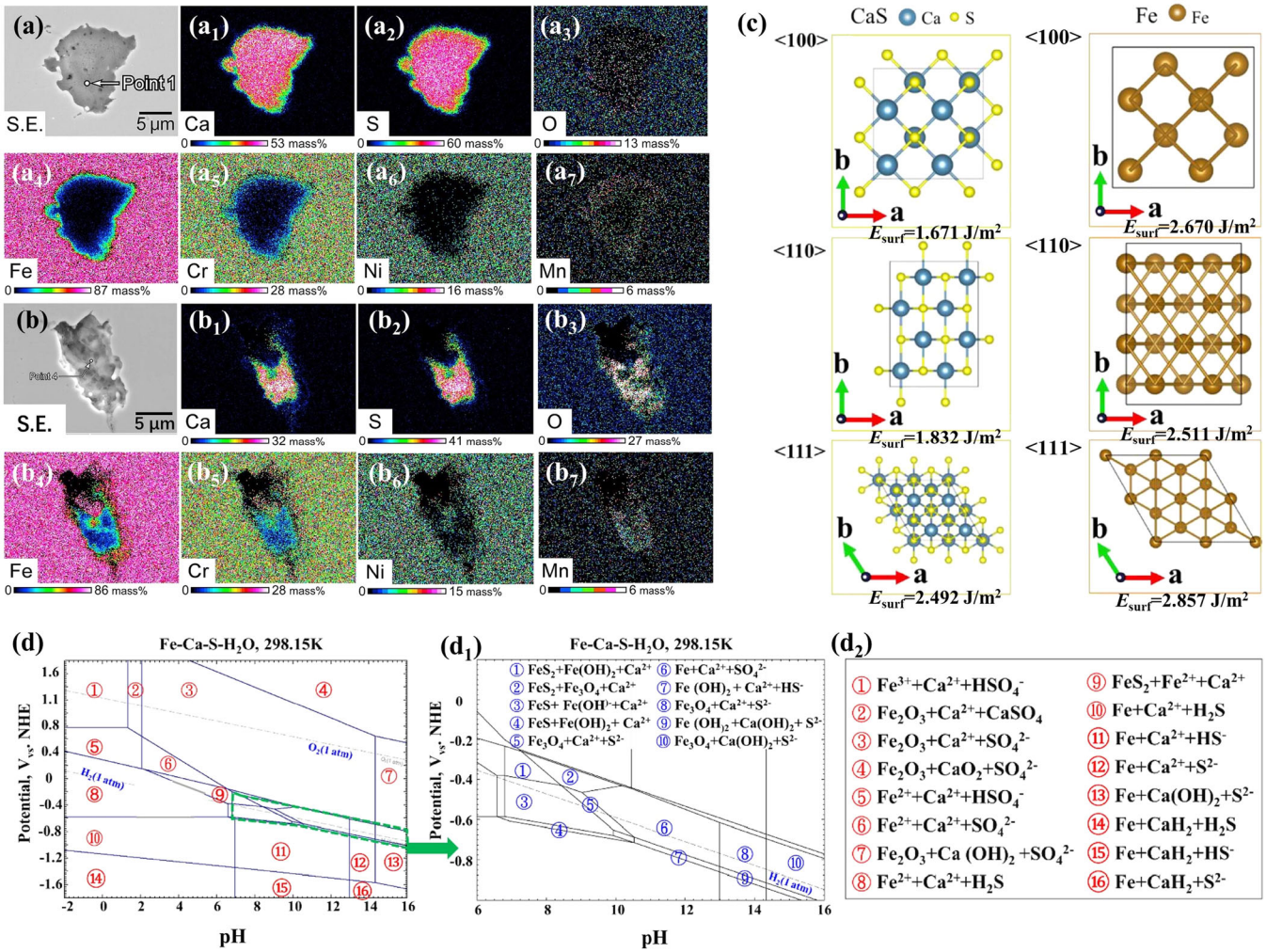

Fig. 6 Degradation behavior and physicochemical properties of CaS. Typical secondary electron (S.E.) images and EDS mapping analysis results of CaS-contained regions in steel (**a**, $\mathbf{a_1}$–$\mathbf{a_7}$) before and (**b**, $\mathbf{b_1}$–$\mathbf{b_7}$) after immersion in 0.1 M NaCl solution for 1 h at ambient temperature. **c** Possible suspected structures and respective surface energy values of CaS and Fe in <1 0 0>, <1 1 0>, and <1 1 1> orientation. **d** Pourbaix diagram of the Fe-Ca-S-H_2O systems at 298.15 K calculated by Factsage software[22,67].

yielding a greater selective dissolution tendency for CaS inclusions[22].

A valuable conclusion can be drawn from the above case, that is Ca treatment still needs to be viewed dialectically from the perspective of optimizing corrosion resistance of steel due to the undeniable double-edged sword effect of CaS itself, even though such procedure is very common in today's metallurgical industry. In other words, albeit the size of the inclusion can be effectively reduced and the shape can also be significantly spheroidized by Ca treatment, the chemical dissolution caused by the severe thermodynamic instability of CaS itself also leads to the formation of pits or microcracks, providing an entrance for the attack of aggressive ions and accelerating the deterioration of localized corrosion.

Anisotropy between inclusions and the matrix

Compared with chemical dissolution of inclusions themselves, preferential dissolution arising from the anisotropy is more of significance. Traditionally, the above anisotropy refers to electrochemical heterogeneity between inclusions and the metal matrix, and the dissolution triggered by inclusions is mostly attributed to the galvanic cell resulting from the potential difference between diverse components in the inclusions or the potential difference between inclusions and the surrounding matrix. From this perspective, active inclusions are nominally classified into two types, namely cathodic inclusions and anodic inclusions, according to the potential difference between target inclusions and the reference. Except for the chemical dissolution of CaS inclusions mentioned in Section 3.1, most sulfide inclusions introduced in literature play a role as anodic phase in steel (especially in stainless steels) and preferentially dissolve electrochemically in aggressive environments[22]. This is because, compared with MnS with a solubility product constant (K_{sp}) value of around 4.2×10^{-14} mol^2 L^{-2} and other sulfides with smaller K_{sp} value, the value for CaS is at least 14 orders of magnitude larger than them and reaches to around 0.6 mol^2 L^{-2} (K_{sp} calculated using Gibbs energies of formation is usually one of the valid parameters to measure the dissolution resistance of inclusions from a perspective of thermodynamic), implying that, aside from CaS, other typical sulfides are less likely to undergo chemical dissolution[68].

In consideration of highest probability of MnS inclusions in various kinds of steels, here we still mainly take it as a typical case and summarize some relevant information extracted from studies in the recent years. It is extensively believed that Mn-rich sulfide inclusions are more favorable to localized corrosion than inclusions abound in Fe, thus it is often considered as a kind of anodic inclusions. However, Dong et al.[69] revised the above

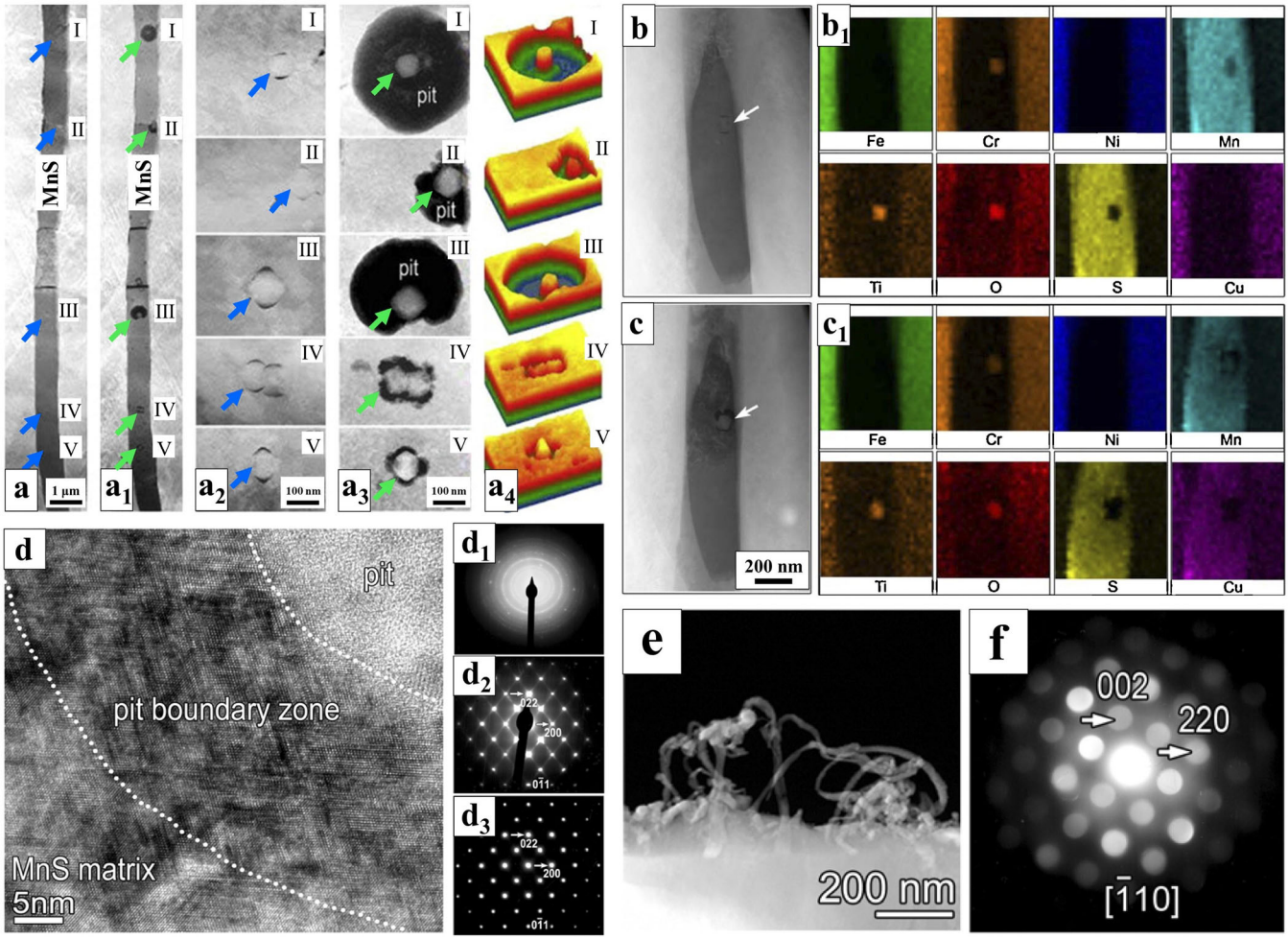

Fig. 7 Corrosion evolution and corresponding characterization of MnS-containing inclusions in aggressive condition. a, **a**$_1$, **a**$_2$, **a**$_3$ HAADF images and its partial enlarged views at various locations showing: **a**, **a**$_1$ An MnS inclusion section in stainless steel, where different positions containing MnS inclusions **a**, **a**$_2$ before and **a**$_1$, **a**$_3$ after exposure in 1 M NaCl solution for 45 min are labeled with I, II, III, IV, and V, and marked with blue and green arrows, respectively. **a**$_4$ Three-dimensional reconstruction morphology of each domain after corrosion. Morphology and elemental distribution results of MnS inclusions in stainless steel alloyed with Cu element **b**, **b**$_1$ before and **c**, **c**$_1$ after immersion in 1 M NaCl solution for 35 min. **d** A high-resolution TEM images of corroded sites containing MnS inclusions and **d**$_1$, **d**$_2$, **d**$_3$electron diffraction patterns taken in the **d**$_1$ dissolution pit, **d**$_2$ at the pit boundary and **d**$_3$ the region far away from the pit, respectively, after immersion in 1 M NaCl solution for 35 min, **e** a zoom-in image of the produced Cu_2S nanowires around the pit and **f** a NBED pattern taken along the [−1 1 0] direction of Cu_2S[66,80].

conclusions based on their experiments, and they believed that MnS inclusions usually play a role as anode in stainless steel, but tend to be cathode in low alloy steel. Besides, the S element in sulfide inclusions in turn accelerates cathodic and anodic reactions, these two factors synergistically render the formation of pitting initiation sites at MnS inclusions in steel[70].

In a very classic work, Ma and his team[66] demonstrated unprecedentedly the origin of preferential dissolution of MnS inclusions in stainless steel by using a high resolution transmission electron microscope (TEM). Figure 7a illustrates a typical HAADF images of the section containing MnS inclusion in 316F stainless steel, while its partial enlarged views at dissimilar locations (Fig. a$_2$), namely I, II, III, IV and V, also vividly prove that cracks are easy to appear between inclusions and adjacent matrix owing to the difference of thermal expansion coefficient and/or different compressive strength or tensile strength between phases and matrix[23]. After exposure in 1 M NaCl for 45 min, the formation of local pit at MnS inclusions is clearly observed (Fig. 7a$_1$–7a$_3$), indicating that MnS inclusions indeed tend to trigger localized corrosion of the metal matrix in aggressive environment as described in many literature[26,70–79]. Combining the three-dimensional reconstructed stereogram further (Fig. 7a$_4$), numerous residual undissolved nano-sized cores can also be noticed in the pit areas with black contrast. Moreover, evidence from composition analysis supports that these residual inclusions are mainly $MnCr_2O_4$ precipitates. With the computation results of the First-principles calculations, they further confirmed that "single-grained" MnS inclusions occurred in the steel are, in general, structurally and compositionally inhomogeneous, while the interface between these fine precipitates with size of several tens of nanometers and MnS inclusions are expected to be a place where initial dissolution initiates with the effect of nano-galvanic cells, and then the dissolution gradually expands outward resulting in forming pits. Also, another similar work led by Ma and his partners[80] manifests that alloying copper (Cu) elements tend to be enriched in the boundary zone of the pits during the dissolution of MnS inclusions in an aggressive conditions (Fig. 7b–7c$_1$). What's more, the high-resolution TEM images of corroded sites (Fig. 7d) and the corresponding electron diffraction patterns (Fig. 7d$_1$–7d$_3$) taken in diverse regions, namely in the pit boundary zone, dissolution pit and the region far away from the pit, after corrosion also prove the results of EDS that element Cu is abound in the area

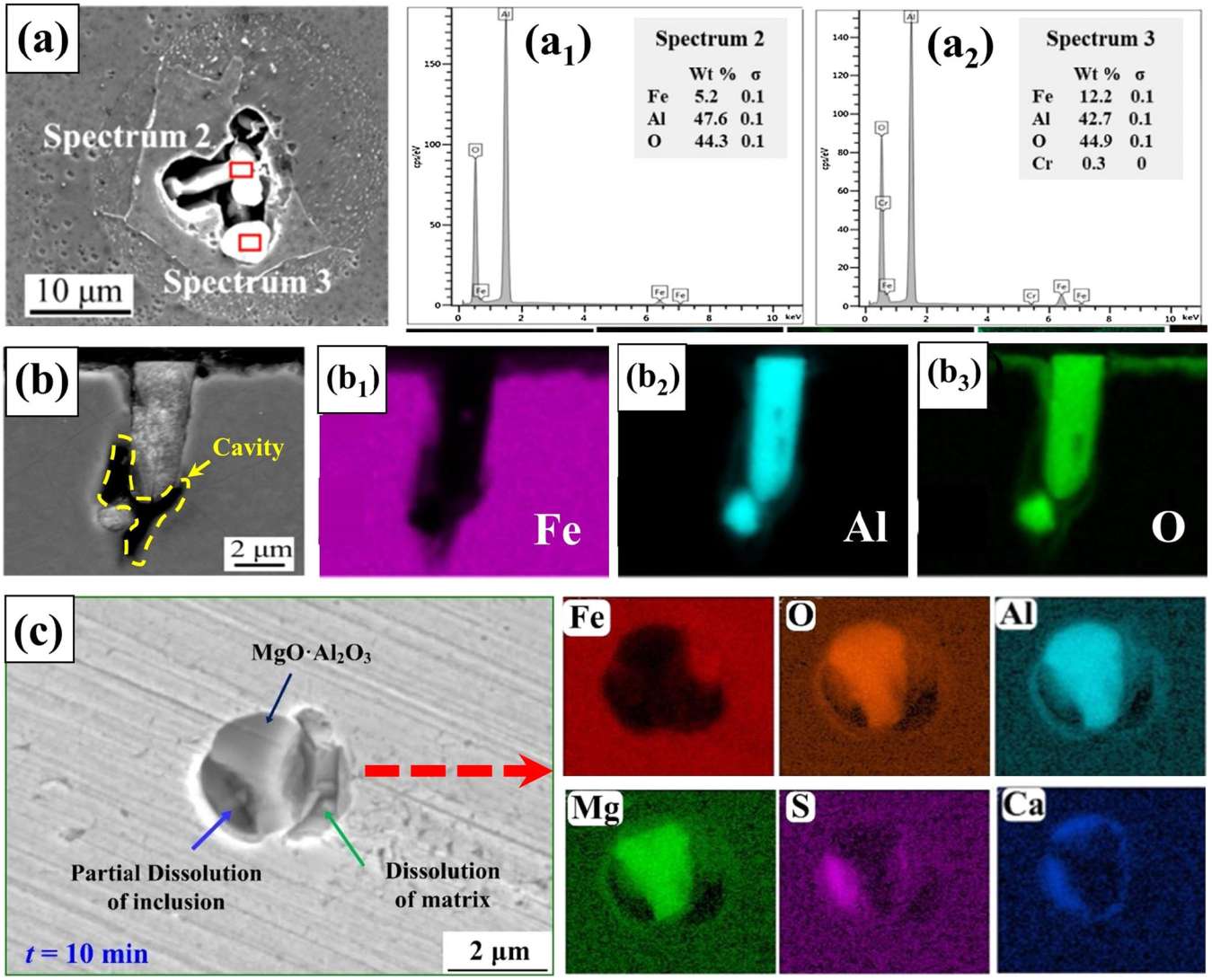

Fig. 8 Corrosion behavior and composition variation of Al_2O_3-containing inclusions in steel. a, **c** Typical SEM images. **b** Cross-sectional images and (**a_1**, **a_2**, **b_1**, **b_2**, **b_3**) corresponding element distribution of the steel containing oxide spinel inclusions (Al-killed steel containing Al_2O_3 inclusions immersed in 1 M NaCl + 0.5 M Na_2SO_4 + 0.5 M $CaCl_2$ for 30 min was shown in **a**–**b_3**, while X70 steel containing complex $xCaS{\cdot}yMgO{\cdot}zAl_2O_3$ inclusions immersed in 0.0111 M $CaCl_2$ + 0.0468 M NaCl + 0.0142 M Na_2SO_4 + 0.0197 M $MgSO_4{\cdot}7H_2O$ + 0.0293 M KNO_3 + 0.0151 M $NaHCO_3$ for 10 min was depicted in **c**) after removal of corrosion product[24,84].

near the pit, in which a high-density Cu [1 1 1] stacking faults and characteristic diffraction spots can be well observed, this interesting phenomenon is also reported in other works[24]. Besides, combined with the accelerated experiments, the other prominent finding in this work is the monitoring of generation of Cu_2S nanowires during the dissolution of MnS inclusions (Fig. 7e, f), which directly provides reliable experimental evidence for the complexity of the dissolution of inclusions. In addition to all of the above, a careful inspection of Fig. $7a_2$ and $7a_3$ suggests that corrosion of metal matrix in the closest vicinity of the inclusion also eventuated. By comparing and observing the dissolution process of massive MnS inclusions, Kelly[81] figures the reason for the above phenomenon is that the by-products, such as HS^-, H^+ and etc., produced after the local dissolution of MnS inclusions hinder the repair of the passive film on the surface of the substrate and drive the matrix exposed in an activated state. Nonetheless, there are still other inconsistent opinions, which will be discussed in the following section. Apart from the archetypal sulfide inclusions, localized corrosion induced by oxide spinel and nitride-type cathodic inclusions in steel is also very common.

Nowadays, some newly-designed types of steels, with superior performance for some specific purposes, are not featured by the sulfide inclusions anymore. Citing aluminum killed steel as a case in point, it is designed by reducing C content and by addition of alloying element Al and has been extensively employed in automobile industry or household appliances[82]. Notably, alumina clusters as main defects are responsible for anisotropy or cracks in aluminum-killed steel, which undoubtedly weakens the properties of steel[83]. Li et al.[24] reported that Al_2O_3 inclusions did not obviously dissolve but the matrix abutting to the inclusions dissolved preferentially already during immersion, when they exposed the Q460NH Al-killed steel containing Al_2O_3 inclusions in a chloride-containing electrolyte for 30 min and removed surface corrosion products (Fig. 8a–$8a_2$). Supports from cross-section images (Fig. 8b–$8b_3$) reveal that chemical stability of cathodic Al_2O_3 inclusions is higher, whilst the cavity left by localized corrosion under the inclusions provides appropriate conditions for the longitudinal expansion of corrosion.

Still, oxide inclusions containing merely one component are always rare in steel. Conversely, inclusions abound in multiple

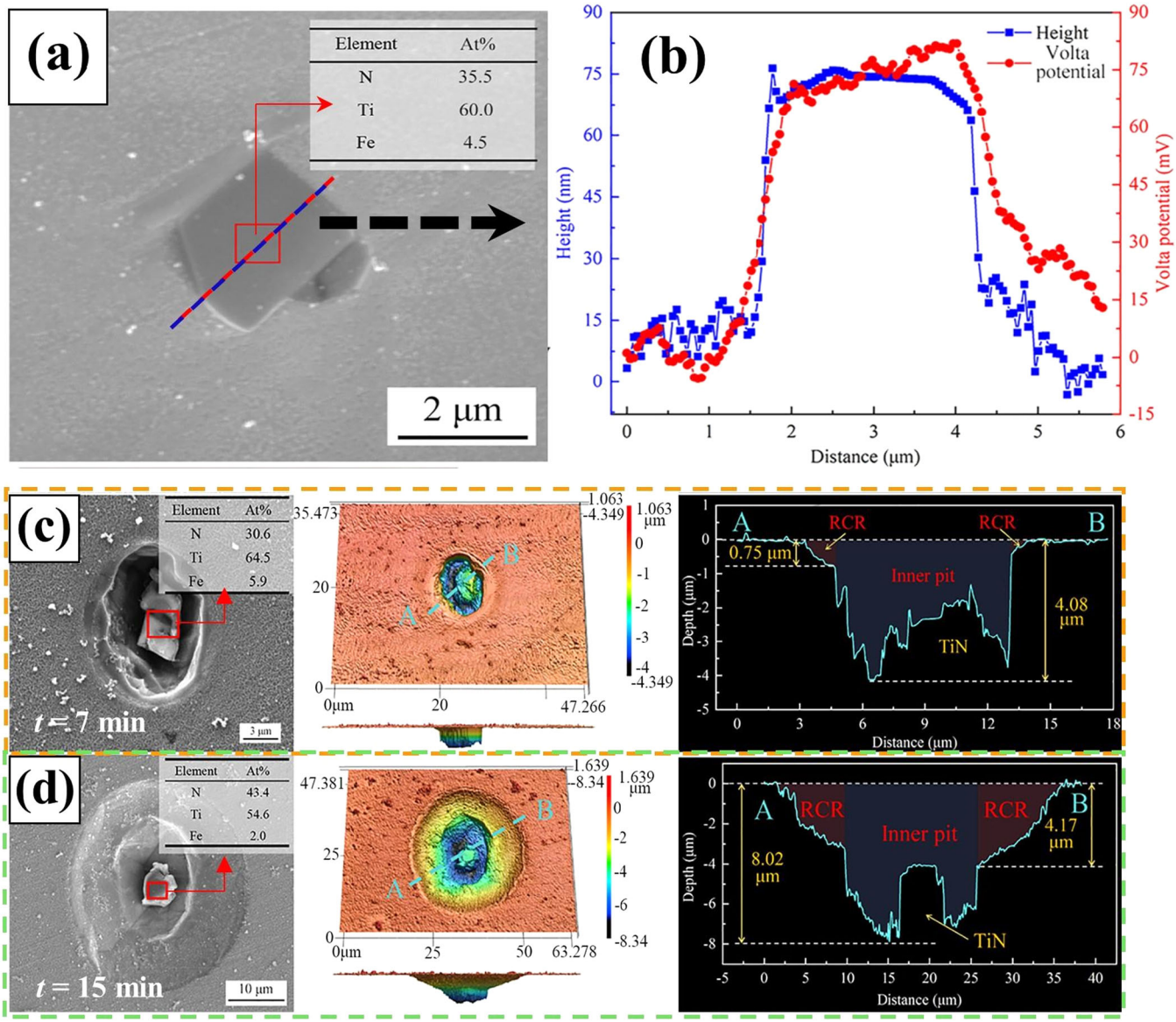

Fig. 9 Typical morphology, properties and corrosion performance of TiN inclusions in interstitial free steel. a SEM images of TiN inclusions in interstitial free steel. **b** Morphology and potential results of line profile in the same region from **a**. **c**, **d** Ex-situ SEM morphological observation of corrosion pit induced by TiN inclusions with time in 0.1 M NaCl solution after removal of corrosion product: **c** 7 min and **d** 15 min. Corresponding three-dimensional images and cross-section of the corrosion pit are illustrated on the right[87].

components are more common. For example, xCaS yMgO $z$$Al_2O_3$ inclusion is typical one, which ubiquitously exists in diverse steels and is usually a by-product of impurity removal. Gui et al.[84] found that apart from the preferential dissolution of CaS portions and partial steel matrix contiguous to the target inclusions, the remaining components of MgO-Al_2O_3 still exist after exposure in a mixed simulated solution for 10 min based on the S.E. images and EDS analysis results (Fig. 8c), when they investigated the dissolution kinetics of the sulfide-oxide complex inclusions in X70 steel. For the reaction activity of CaS, which has been described in detail previously, while Tyurin and Reformatskay[85,86] also clarified in their works that CaS is the most easily decomposed type among various typical inclusions. Besides, the resulting remnant indirectly offers a good support for Li's conclusions[24] namely oxide spinel inclusions are electrochemically inactive with respect to metal matrix and tend to stably exist even in corrosive environment.

Regarding nitride-type cathodic inclusions, as illustrated in Section 2.2, TiN is also a kind of representative inclusions and has significant detrimental effects on the localized corrosion of steel. A typical S.E. images and the corresponding morphology as well as potential results of TiN inclusions in interstitial free steel are shown in Fig. 9a, b[87]. Consistent with what we have previously stated, TiN inclusions are faceted cubic shape with sharp edges and angles (Fig. 9a), whilst its higher height and Volta potential than the base metal are very remarkable from the scanning kelvin probe (SKP) results (Fig. 9b), accounting for the increasing risk of galvanic corrosion between TiN inclusions and matrix adjacent to it. As expected, the topography after immersion in 0.1 M NaCl solution for 7 min and 15 min shows an obvious ring-like corroded region, while the corresponding cross-section images manifest the stepped shape of corrosion pit, indicating that the development of corrosion pit is mainly for the internal vertical expansion and the surrounding epitaxial expansion (Fig. 9c, d).

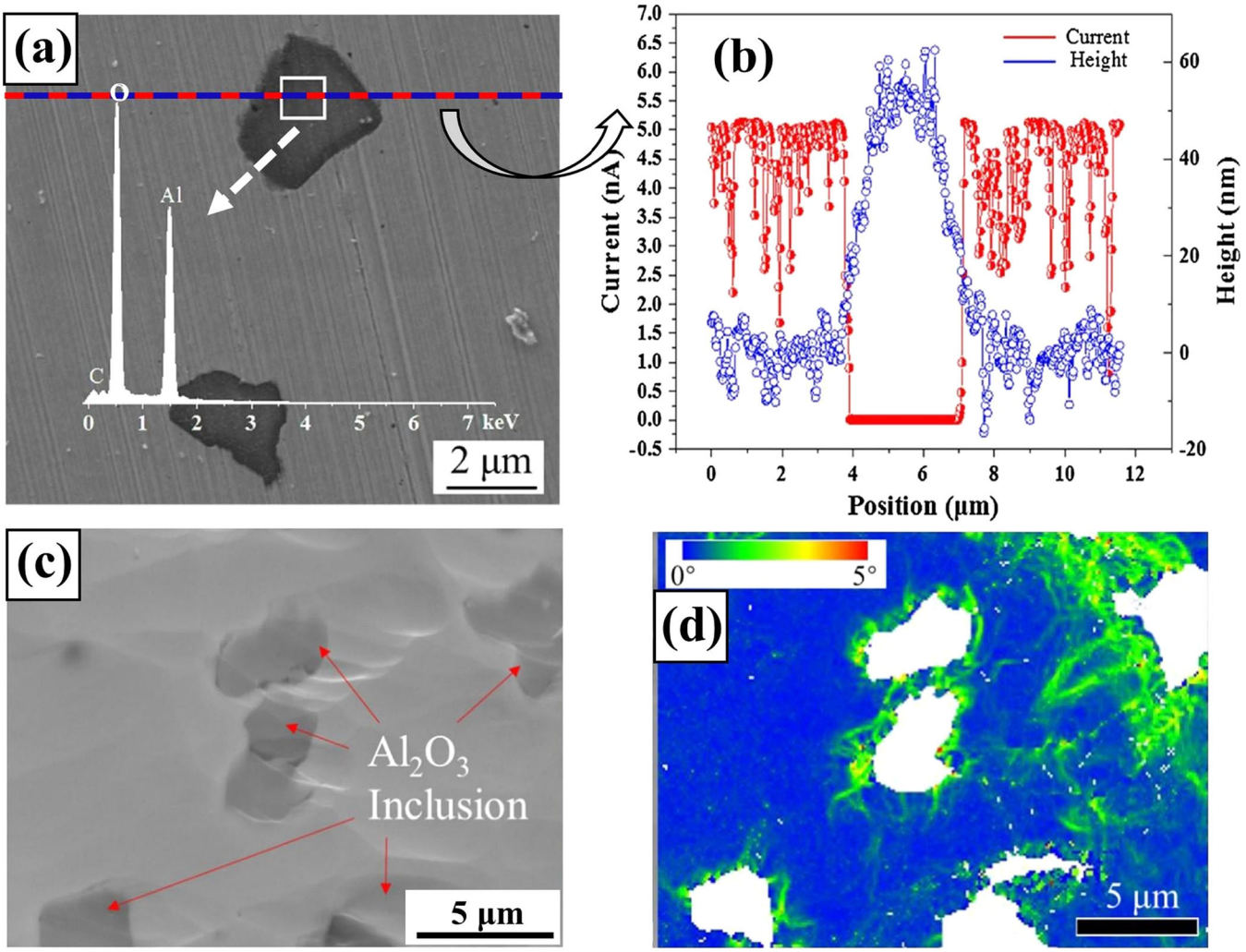

Fig. 10 Morphology and properties of Al_2O_3 inclusions in Al-killed steel. a SEM images of Al_2O_3 inclusions in Al-killed steel. **b** Morphology and conductive analysis results of line profile in the same region shown in **a**, gained with a potential of +6.0 V applied to the tip. EBSD images of a region containing Al_2O_3 inclusions: **c** SEM images and **d** the corresponding KAM map of the same region shown in **c**[24].

As stated above, the local preferential dissolution of the matrix adjacent to the inclusions in most cases is resulted from the potential difference. Also, it seems to be a consensus that the initial place of corrosion usually occurs at the direct contact sites of heterogeneous conductive materials of distinct potentials, and the dissolution tends to expand to the side with more negative corrosion potential. Nevertheless, the conductivity of inclusions is commonly neglected in most previous studies, and researchers focus more on the potential difference between inclusions and metal matrix.

Additionally, due to the surface potential measured by SKP tests is generally positively correlated with the corrosion potential of the materials, especially for metallic materials. Therefore, in some past works, the local matrix exhibiting higher preferential dissolution tendency is often randomly associated with its lower surface potential based on the experimental phenomenon[88,89]. As a result, the inaccurate recursive relationship that inclusions form a galvanic coupling with the matrix adjacent to it as well as the matrix with a lower surface potential serving as the cathode phase preferentially dissolves is concluded and circulated.

Although the above conventional conclusions are indeed applicable to localized corrosion triggered by a part of inclusions. Yet it has been questioned by some scholars recently, since it is contrary to their experimental results. Furthermore, the accumulation of corrosion products on the interphase during the corrosion evolution may also distort the reliability of the initial judgment on the polarity of inclusions based on the surface potential value measured by SKP tests.

Interphase defects-triggered selective dissolution

The most classic work in the skeptical attitude towards the above views is the breakthrough achievements gained by Li et al.[24] in the study of localized corrosion induced by Al_2O_3 inclusions in Al-killed steel in 2018. By employing a series of advanced characterization approaches including electron backscatter diffraction (EBSD) and current sensing atomic force microscopy, this study intuitively shows the insulating property of Al_2O_3 inclusions (Fig. 10a, b), and negates the applicability of traditional galvanic coupling theory in localized corrosion triggered by Al_2O_3 inclusions. In addition, a more rational reason that a higher density of dislocations in matrix adjacent to inclusions for inducing local selective dissolution was innovatively put forward based on the kernel average misorientation (KAM) map from EBSD results (Fig. 10c, d), since they suppose that the dislocations correspond to higher lattice distortion, thus regions with high dislocation density are thermodynamically unstable and more susceptible to corrosion than elsewhere. Still, we have mentioned in our previous work that above conclusions are creative but

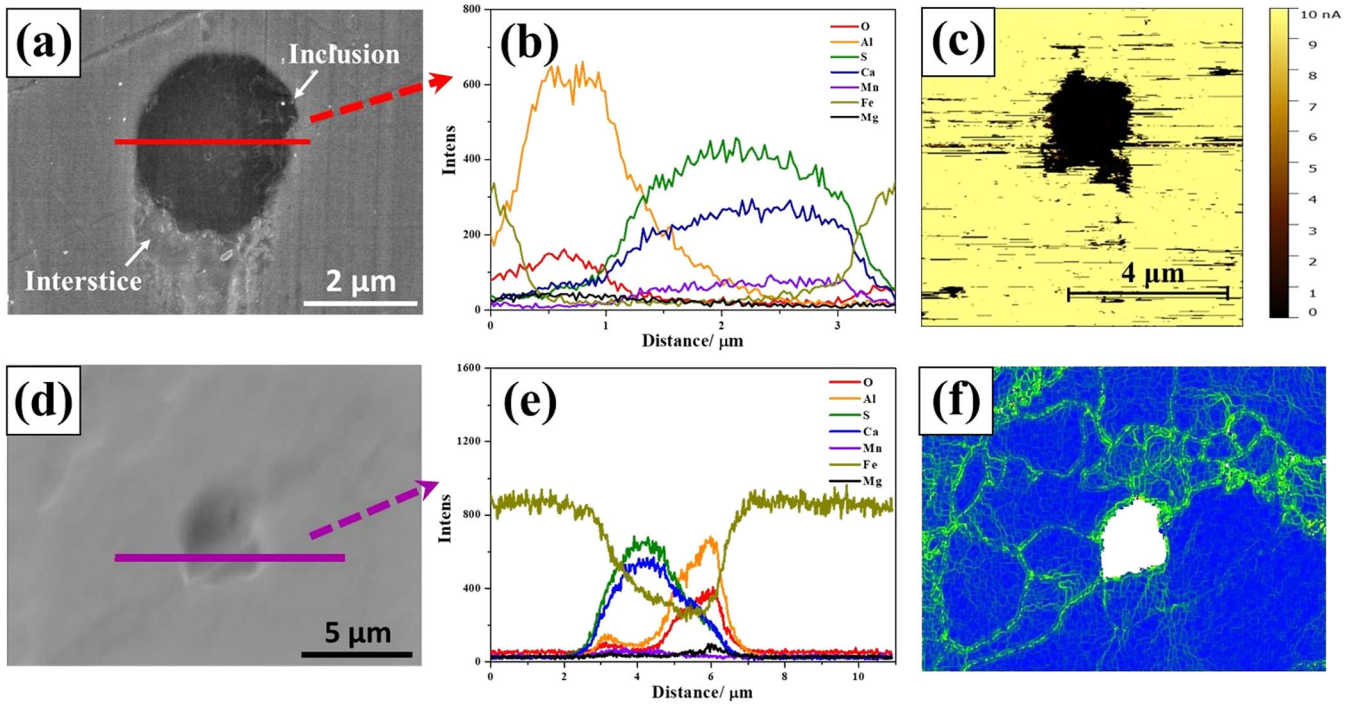

Fig. 11 Morphology and properties of (Al, Mg, Ca, Mn)-oxy-sulfide inclusions in weathering steel. a, **d** SEM images of target (Al, Mg, Ca, Mn)-oxy-sulfide inclusions and its corresponding element distribution results. **c** Conductive map of the target inclusion in the same region shown in **a**, obtained with a potential of +5.0 V applied to the tip. **f** The KAM map of the same region shown in **d**[90].

somewhat evident, because it is very unlikely for pure Al_2O_3 inclusions, a material with high electrical volume resistance around 10^{15} Ω at room temperature, to trigger localized corrosion through galvanic cell[44,45,90]. Meanwhile, Al_2O_3 is commonly known as corundum due to its ultra-high hardness, whereby it also seems obvious that the serious defects are inclined to be introduced to the direct contact sites between inclusions and matrix during steel rolling process, thanks to the difference of deformation coefficients.

In our previous work on inclusion in weathering steel, we have also tried to explore the reason of localized corrosion triggered by more common complex (Al, Mg, Ca, Mn)-oxy-sulfide inclusions[90]. As exhibited, selective target inclusions are approximately ellipsoidal in shape (Fig. 11a, d), while the characteristics of element distribution illustrate that its composition is mainly (Ca, Mn)-sulfides portion and (Ca, Al, Mg)-oxides portion (Fig. 11b, e). Interestingly, as with inclusions containing pure Al_2O_3, the monitored current value of inclusions at the same location shown in Fig. 11a also approaches to Picoampere (Fig. 11c), indicating the poor conductivity of the target inclusion. This depicts that the galvanic coupling theory also fails in explaining the localized corrosion induced by the current complex target inclusions. (Note that the surface potential distribution of the selected inclusions and matrix and their localized corrosion evolution in aggressive condition are similar to those reported in most previous works, namely the potential of (Al, Mg, Ca, Mn)-oxy-sulfide inclusions is relatively higher than that of the matrix, and the matrix near the inclusions preferentially dissolves in corrosive environments, thus this part of the results is not presented here. For more information, please refer to literature[90]). In conjunction with the above experience, EBSD test was further carried out on the target inclusions and the corresponding KAM map fully demonstrated that the high dislocation density around the inclusions is the same as that in the grain boundary (Fig. 11f), this result is similar to the work of Li et al.[24] and implies that there is presence of serious lattice distortion around the selected target inclusions, leading to thermodynamic instability of the local matrix.

The above similar conclusions have also been reported in localized corrosion triggered by TiN-containing inclusions, but the situation is somewhat more complicated. For example, in the investigation on mechanism of localized corrosion triggered by TiN-containing inclusions in high strength low alloy steel, Yang et al.[22] not only observed the occurrence of preferential localized corrosion of the metal matrix adjacent to the target inclusions, but unexpectedly uncovered that residual $xMgO{\cdot}yAl_2O_3{\cdot}TiN$ remains stable in the sample after immersion in a typical corrosive solution (1 M NaCl + 0.5 M Na_2SO_4 + 0.5 M $CaCl_2$) even up to 12 h, although TiN exhibits anodic properties because of the lower potential of TiN portion in the target $CaS{\cdot}xMgO{\cdot}yAl_2O_3{\cdot}TiN$ inclusions than that of the matrix. Besides, the good conductivity of TiN portion also provides a good basis for its role as the anode in the galvanic coupling (Fig. 12c, d, f, g). For the selective dissolution of matrix, the authors pose the possible speculation similar to that drew from Figs. 10, 11, according to KAM diagram depicted in Fig. 12i. Surprisingly, the dissolution behavior of TiN portion is completely opposite to its physical properties. After careful detailed phase analysis, it was unexpectedly discovered that a thin layer of TiO_2 passive film featured *n*-type semiconducting nature covered the surface of TiN portion. Also, the First-principles calculation results imply that TiN possesses higher reaction activity. After integrating and comparing all the objective results, the author confirmed the speculation that TiN can indeed react with dissolved oxygen in the solution to generate TiO_2, which supports the rationality of the detection results of TiO_2 on the surface of TiN inclusions. For the abnormal behavior of preferential dissolution of the matrix with higher potential in the TiN/matrix galvanic coupling, the author also gave a corresponding explanation. It is well known that electrons are restrained to cross the two-phase interface in terms of *n*-type semiconducting unless the potential go down to the flat band potential, hinting that the generation of TiO_2 results the reversal of heteropolarity of

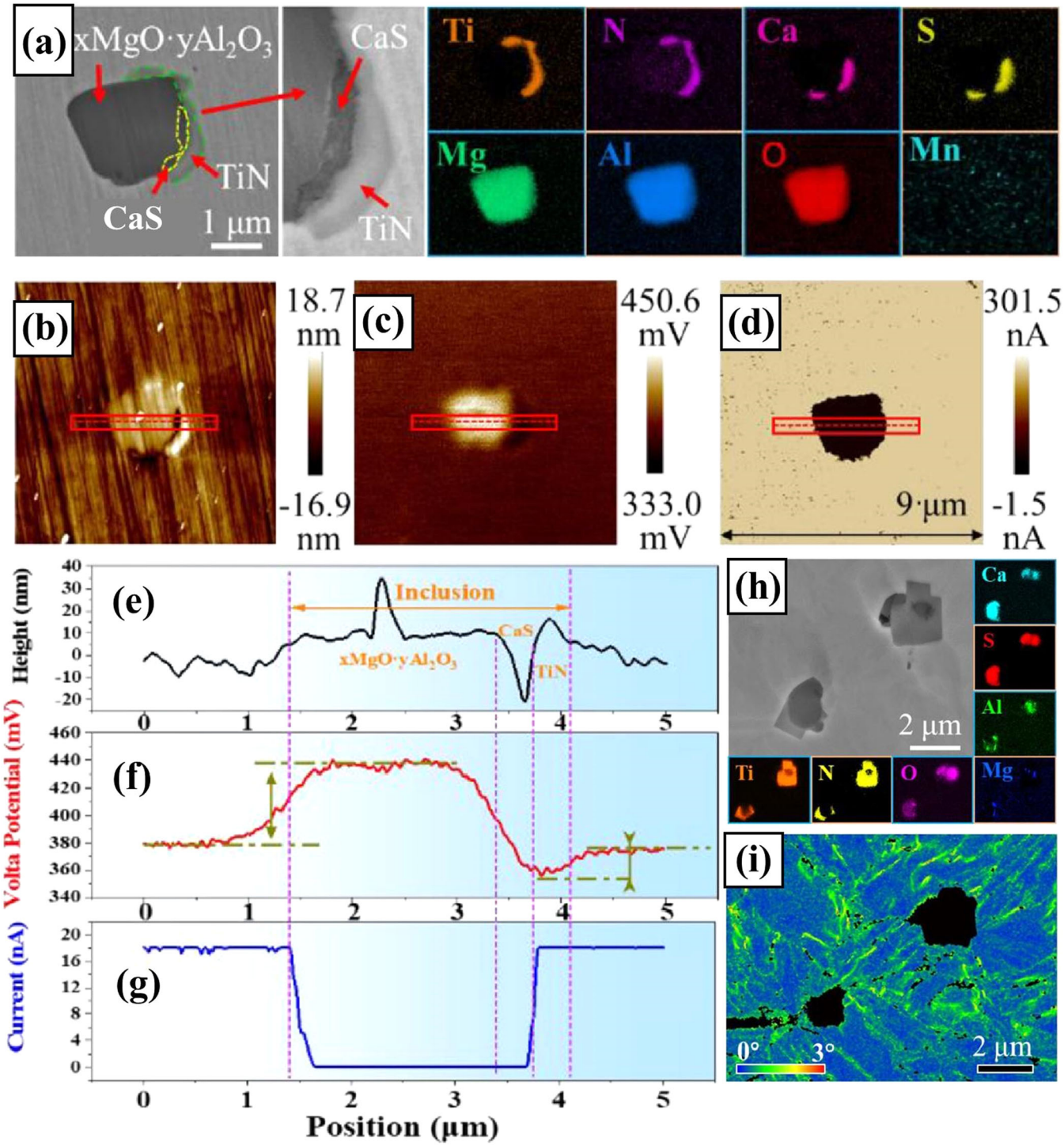

Fig. 12 Multiple characterization results of CaS·*x*MgO·*y*Al_2O_3·TiN inclusions. a, **h** Morphology of typical target CaS·*x*MgO·*y*Al_2O_3·TiN inclusions and the corresponding element distribution. **b** Topography map, **c** potential map and **d** conductive map of the same region shown in **a**. **e**–**g** The strip profile analysis results of the target inclusions shown in **a**. **i** The KAM map of the same region shown in **h**[22].

TiN/matrix galvanic coupling and in turn accelerates the corrosion of surrounding matrix to a certain degree[91–93].

From the previous quintessential examples, it has already been known that, aside from the local selective dissolution of the adjacent matrix triggered by the conductive inclusion, the higher thermodynamic instability and corrosion sensitivity resulted from the serious lattice distortion from the two-phase contact sites to the matrix side are the chief agents for the insulating inclusions-induced localized corrosion. Nonetheless, another innovative work studied by Li and Moelans[23] provides the third explanation for the above situation when they paid attention to the effects of rare-earth elements modified inclusions (Fig. 13a, c, e) on initialization of localized corrosion of pipeline steels in NaCl solution, whilst reports on modifying the corrosion resistance of steel by adding rare-earth elements have also been introduced elsewhere[94–99]. In this investigation, the bandgap values (E_g) of $LaAl_2O_3$ obtained by experiment and calculation is around 5.47 eV and 5.60 eV, respectively (Fig. 13b), while materials with E_g smaller than 5 eV

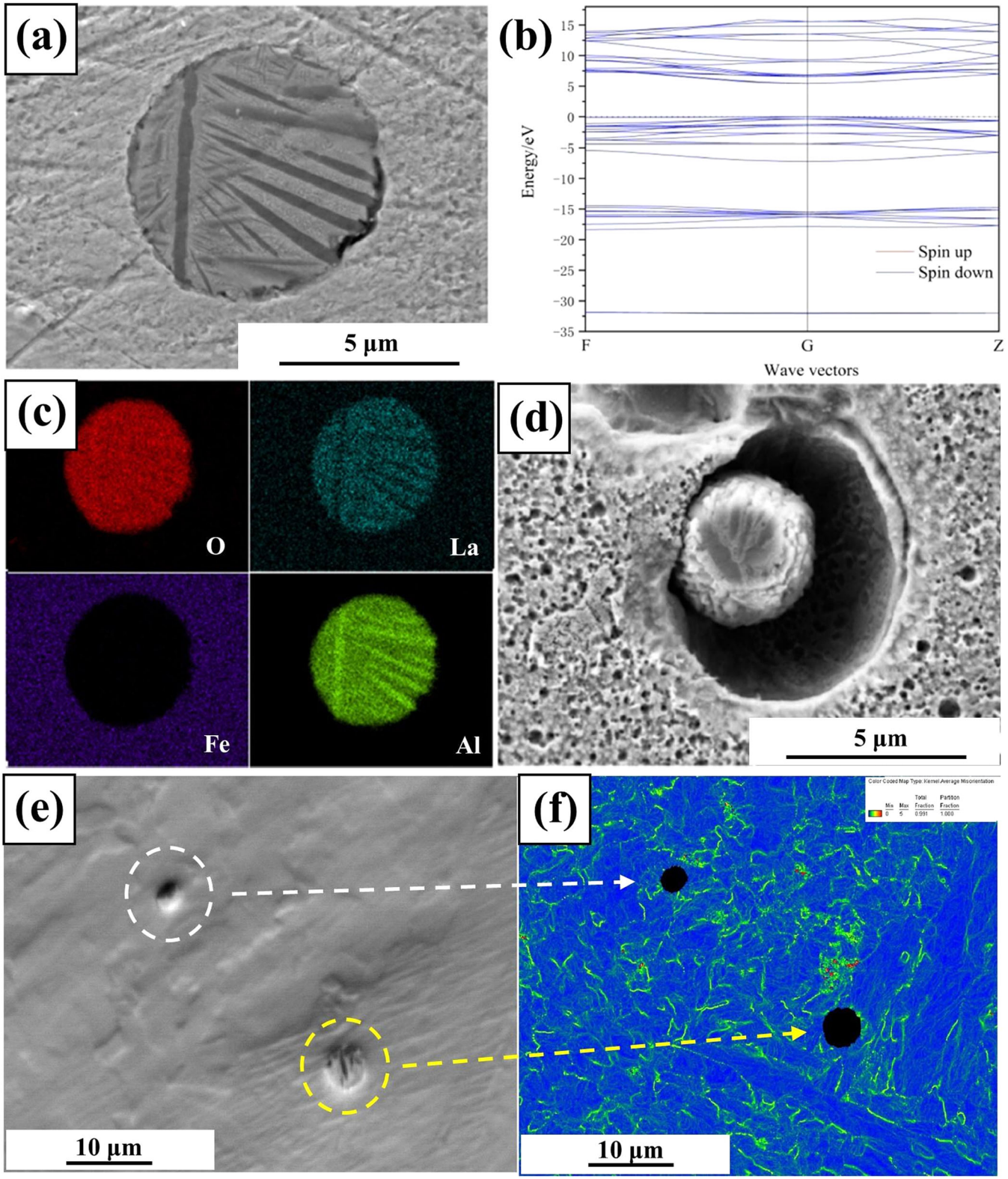

Fig. 13 Characterization and corrosion test for $LaAlO_3$ inclusion. a SEM photographs and **c** the element distribution of target $LaAlO_3$ inclusion. **b** Typical energy band structure analysis results of $LaAlO_3$ inclusion. **d** Morphology observation of the same region as **a** after immersion in 0.62 M NaCl solution for 80 min. EBSD images of a region containing $LaAlO_3$ inclusions: **e** SEM images and **f** the corresponding KAM map of the same region shown in **e**, the white and yellow dashed circles in **e** corresponds to the target inclusions with black contrast shown in **f**[23].

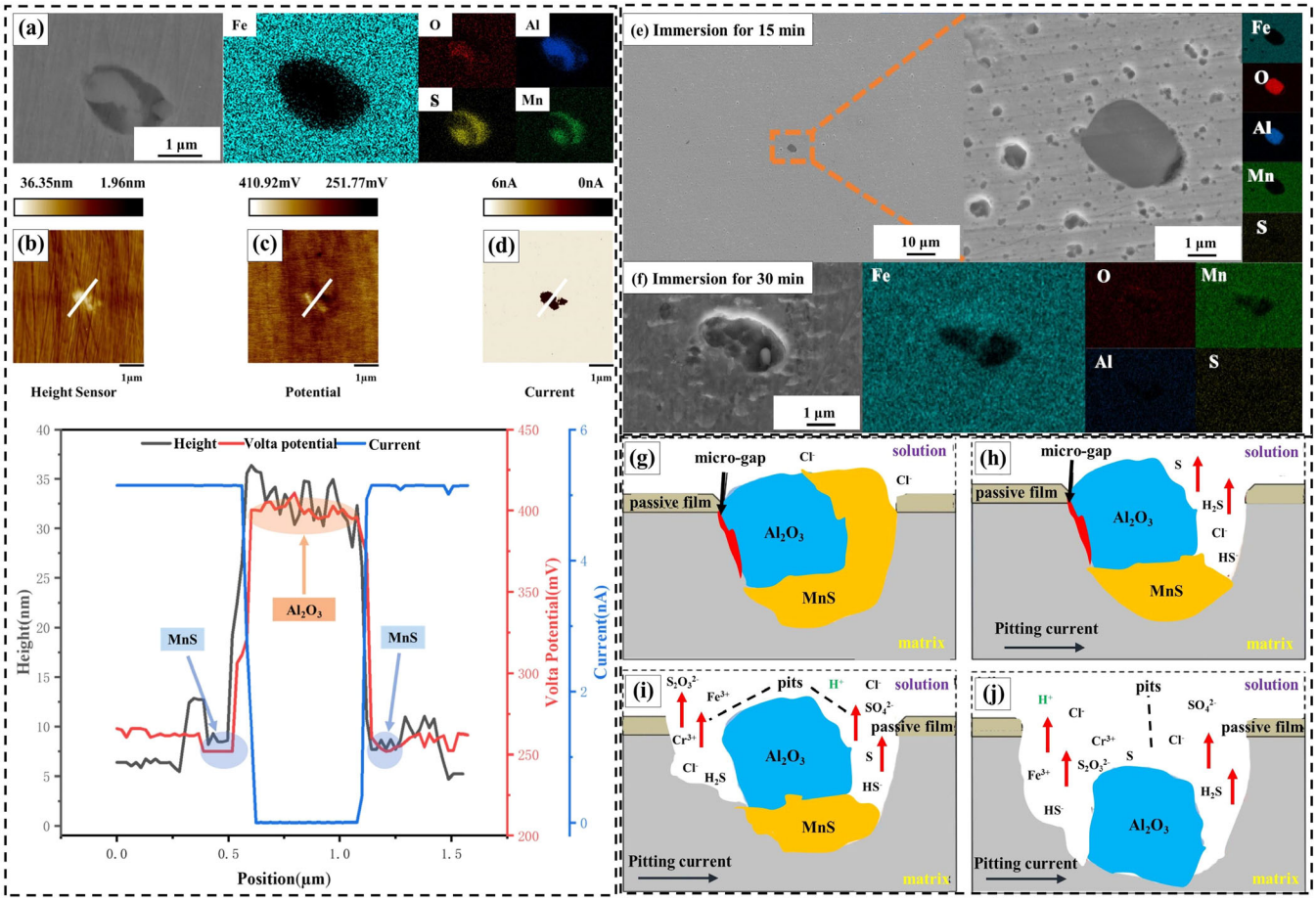

Fig. 14 Characterization measurements and corresponding corrosion evolution diagram for Al_2O_3-MnS inclusions in steel. a–d SEM-EDS and micro-electrochemical measurements of Al_2O_3-MnS inclusions in steel: **a** SEM-EDS images, **b** AFM topography, **c** Volta potential distribution, and **d** current distribution. **e**, **f** Morphology and composition characterization of Al_2O_3-MnS inclusions after immersion in a mixed aggressive solution (1 M NaCl + 0.5 M Na_2SO_4 + 0.5 M $CaCl_2$) for **e** 15 min and **f** 30 min. **g–j** Schematic diagram of the pit initiation and propagation evolution triggered by Al_2O_3-MnS inclusions[16,21].

are regarded as conductor, indicating that $LaAl_2O_3$ inclusions pertain to insulator. Interestingly, local preferential dissolution of the matrix adjacent to the inclusion was indeed observed after exposure in corrosive solution (0.62 M NaCl) for 80 min (Fig. 13d), whereas the weak dislocation density of the matrix around the inclusions also can be reflected from the KAM map (Fig. 13f), which seemed to be contradictory. By comparing with the corrosion evolution of another rare-earth element modified inclusion without apparent microcrevices at the contact sites, they speculated that the localized corrosion triggered by the target $LaAl_2O_3$ inclusions arises from the accumulation of aggressive ions at the microcrevices, where the degradation of passive film easily occurs.

Through multi-dimensional comparison of the above classic cases, it vividly and concretely shows that the localized corrosion induced by inclusions in steel is much more intricate than the conventional mechanistic realization based on the observation results after immersion and the unpersuasive surface potential data obtained from the initial tests. On the contrary, the microcrack and/or potential difference between inclusions and matrix as well as the lattice distortion of the adjacent matrix may be the prerequisites for triggering the localized corrosion in the initial stage.

So far, it can be well recognized that galvanic corrosion theory cannot be arbitrarily employed to explain the inclusion-triggered localized corrosion without experimental confirmation on any occasions. On the top of that, evolution of inclusion-triggered corrosion form is also a crucial concern that needs special attention. Alternatively, the corrosion mechanism of non-galvanic corrosion is believed to be clarified based on the previous illustration, thus here we desire to focus on the possible variation in corrosion form during the galvanic corrosion induced by a class of conductive inclusions. To the best of our knowledge, in addition to the TiN inclusions mentioned in Fig. 12 as a typical type of inclusions which might change the corrosion form due to its reversal of polarity during corrosion evolution, galvanic corrosion generated by inclusions and matrix also perhaps be changed into other corrosion form attributing to the complete dissolution of some soluble portions. As depicted in Fig. 14, a Al_2O_3–MnS complex inclusion-triggered localized corrosion system involved in some investigations is a representative case in terms of the above situation[16,21]. Volta potential measurement and conductivity test determine the insulating properties of Al_2O_3, and also confirm the illustration in Section 3.2 that conductive MnS inclusions often act as an anode in stainless steel (Fig. 14b–d). Meanwhile, results of EDS show that MnS portion directly borders the matrix, indicating that the prerequisites of galvanic corrosion generated by MnS portions and matrix are satisfied (Fig. 14a). After a series of immersion tests and characterizations, it was found that MnS did preferentially dissolve (the signals of Mn and S elements cannot be detected after 15 min immersion in an aggressive solution). Nevertheless, the localized corrosion triggered by inclusions did not terminate, especially the detection signals of Al and O elements were weak after immersion for 30 min, which fully

suggests that the corrosion form underwent a transition from galvanic corrosion to non-galvanic corrosion during corrosion evolution. To display more intuitively, Dong et al.[16] specially divided above process into four steps by a way of schematic diagram, as shown in Fig. 14g–j.

SUMMARY AND PERSPECTIVE

In this project, we review the source of typical inclusions and provide a detailed summary of recent literature on the causes of localized corrosion triggered by inclusions. The removal of impurity elements and alloying for optimizing material properties are the two fundamental factors for the introduction of inclusions in steel. Here, we distinguish them by the name of secondary-derived inclusions and nascent inclusions. In addition, in terms of inclusions-induced localized corrosion, by means of various advanced technologies together with theoretical calculations, the chemical dissolution of some inclusions thanks to their higher reactivity and the electrochemical anisotropy between conductive inclusions and adjacent matrix, and thermodynamic instability occasioned by structural defects in the matrix around insulating inclusions are the most essential driving forces for the initialization of localized corrosion. Prime examples are respective severe chemical/electrochemical dissolution of CaS and/or MnS in single or complex component inclusions and local selective dissolution in aggressive environments of matrix around insulating spinel MgO, Al_2O_3 and/or $MgO{\cdot}Al_2O_3$ inclusions due to local higher lattice distortion. Alternatively, the examples of TiN-containing inclusions studied by Yang et al.[22] fully disclose that the properties of inclusion are favorable to convert with the corrosion evolution, whereby its role in corrosion process cannot be roughly defined only by characterization from TEM, SKP and so forth. New evidence also puts forward boundaries for the application of the classical galvanic coupling theory in localized corrosion triggered by inclusions, and remind those who dedicates to localized corrosion related to inclusions to stay away from the trap of entrenched idea in the subsequent research and pay more attention to the conductivity of the inclusions other than the surface potential, microdefects at direct connect sites as well as the distortion degree of matrix adjacent to inclusions before mechanism interpretation.

Modern physics and chemistry are evolving rapidly, and in-situ or ex-situ detection technologies need to be advanced in parallel to achieve dynamic monitoring of the entire corrosion process. In terms of inclusion-induced localized corrosion, we see amongst the major challenges in the next steps of development as gaining the ultra-high resolution figures and element distribution results of the micro-regions, and of realizing the accurate judgment for the preferential corrosion position of inclusion or local matrix when it is infinitely close to the initial stage. The main driver behind this is based on the discovery that preferential dissolution of inclusions or adjacent matrix also show selective in previous work, indicating that the future studies on inclusion-induced corrosion is expected to be further carried out at the nano-to-atomic scale[100–103]. What's more, the conductivity of target inclusion and the potential difference between inclusions and matrix, and the micro-defects at the contact sites are the prerequisites for triggering localized corrosion in an aggressive condition. It is likely however that in real corrosion system, considering the uncertainty of corrosion evolution trend influenced by the generation of corrosion products, the in-situ spatial resolution corrosion detection method with time-scales will also be required to achieve the correct and optimal cognitive solution. In addition, the selection and proportion of alloying elements in metallurgical industry are two key factors, while the knowledge of localized corrosion and the design of new materials with satisfied corrosion resistance certainly complement each other. In today's booming environment of computing science, again, we believe that selecting an appropriate and efficient computing model combined with hardware, software techniques and professional knowledge can not only greatly shorten the time cost of scientific research and improve the work efficiency, but provide an effective strategy for correctly understanding the inclusion-induced localized corrosion. In the meantime, a rational cognition for such corrosion phenomenon will also undoubtedly benefit material scientists and engineers to reasonably select the types of alloying elements during material design.

DATA AVAILABILITY

The datasets generated and/or analyzed during the current study are available from the corresponding author upon reasonable request.

Received: 4 July 2022; Accepted: 8 September 2022;
Published online: 26 September 2022

REFERENCES

1. Shao, W. et al. Cohesion properties and tensile cracking behavior of CrN coating on γ-Fe matrix by first principles study. *Appl. Surf. Sci.* **563**, 150279 (2021).
2. Cheng, X. Q., Jin, Z., Liu, M. & Li, X. G. Optimizing the nickel content in weathering steels to enhance their corrosion resistance in acidic atmospheres. *Corros. Sci.* **115**, 135–142 (2017).
3. Wang, Y. F., Cheng, G. X. & Li, Y. Observation of the pitting corrosion and uniform corrosion for X80 steel in 3.5 wt.% NaCl solutions using in-situ and 3-D measuring microscope. *Corros. Sci.* **111**, 508–517 (2016).
4. Xu, W. H., Han, E. H. & Wang, Z. Y. Effect of tannic acid on corrosion behavior of carbon steel in NaCl solution. *J. Mater. Sci. Technol.* **35**, 64–75 (2019).
5. Morcillo, M. et al. Atmospheric corrosion of weathering steels. Overview for engineers. Part I: Basic concepts. *Constr. Build. Mater.* **213**, 723–737 (2019).
6. Liu, B. et al. Effect of tin addition on corrosion behavior of a low-alloy steel in simulated costal-industrial atmosphere. *J. Mater. Sci. Technol.* **35**, 1228–1239 (2019).
7. Hou, B. R. et al. The cost of corrosion in China. *npj Mater. Degrad.* **1**, 1–10 (2017).
8. Li, X. G., Zhang, D. W., Du, C. W., Liu, Z. Y. & Dong, C. F. Materials science: share corrosion data. *Nature* **527**, 441–442 (2015).
9. Gunasegaram, D. R., Venkatraman, M. S. & Cole, I. S. Towards multiscale modelling of localised corrosion. *Int. Mater. Rev.* **59**, 84–114 (2013).
10. Tian, W. M., Du, N., Li, S. M., Chen, S. B. & Wu, Q. Y. Metastable pitting corrosion of 304 stainless steel in 3.5% NaCl solution. *Corros. Sci.* **85**, 372–379 (2014).
11. Zhang, F., Pan, J. S. & Lin, C. J. Localized corrosion behaviour of reinforcement steel in simulated concrete pore solution. *Corros. Sci.* **51**, 2130–2138 (2009).
12. Taryba, M. G. et al. Novel use of a micro-optode in overcoming the negative influence of the amperometric micro-probe on localized corrosion measurements. *Corros. Sci.* **95**, 1–5 (2015).
13. Park, I. J. et al. Pitting corrosion behavior in advanced high strength steels. *J. Alloy. Compd.* **619**, 205–210 (2015).
14. Wu, H. B. et al. Influence of inclusion on corrosion behavior of E36 grade low-alloy steel in cargo oil tank bottom plate environment. *J. Iron. Steel Res. Int.* **21**, 1016–1021 (2014).
15. Hayden, S. C. et al. Localized corrosion of low-carbon steel at the nanoscale. *npj Mater. Degrad.* **3**, 1–9 (2019).
16. Wang, C. G. et al. Effects of rare earth modifying inclusions on the pitting corrosion of 13Cr4Ni martensitic stainless steel. *J. Mater. Sci. Technol.* **93**, 232–243 (2021).
17. Pu, Z. et al. Effect of carbo-nitride-rich and oxide-rich inclusions on the pitting susceptibility of depleted uranium. *Corros. Sci.* **124**, 160–166 (2017).
18. Liu, C. et al. Effect of inclusions modified by rare earth elements (Ce, La) on localized marine corrosion in Q460NH weathering steel. *Corros. Sci.* **129**, 82–90 (2017).
19. Örnek, C. & Engelberg, D. L. SKPFM measured Volta potential correlated with strain localisation in microstructure to understand corrosion susceptibility of cold-rolled grade 2205 duplex stainless steel. *Corros. Sci.* **99**, 164–171 (2015).
20. Zheng, S. Q., Li, C. Y., Qi, Y. M., Chen, L. Q. & Chen, C. F. Mechanism of (Mg, Al, Ca)-oxide inclusion-induced pitting corrosion in 316L stainless steel exposed to sulphur environments containing chloride ion. *Corros. Sci.* **67**, 20–31 (2013).
21. Liu, C. et al. Initiation mechanism of localized corrosion induced by Al_2O_3-MnS composite inclusion in low-alloy structural steel. *Metals* **12**, 587 (2022).
22. Liu, C. et al. New insights into the mechanism of localised corrosion induced by TiN-containing inclusions in high strength low alloy steel. *J. Mater. Sci. Technol.* **124**, 141–149 (2022).

23. Hou, Y. et al. Effects of $LaAlO_3$ and La_2O_2S inclusions on the initialization of localized corrosion of pipeline steels in NaCl solution. *Scr. Mater.* **177**, 151–156 (2020).
24. Liu, C. et al. Role of Al_2O_3 inclusions on the localized corrosion of Q460NH weathering steel in marine environment. *Corros. Sci.* **138**, 96–104 (2018).
25. Liu, C. et al. Synergistic effect of Al_2O_3 inclusion and pearlite on the localized corrosion evolution process of carbon steel in marine environment. *Materials* **11**, 1–15 (2018).
26. Avci, R. et al. Mechanism of MnS-mediated pit initiation and propagation in carbon steel in an anaerobic sulfidogenic media. *Corros. Sci.* **76**, 267–274 (2013).
27. Cao, Y., Li, G., Hou, Y., Moelans, N. & Guo, M. DFT study on the mechanism of inclusion-induced initial pitting corrosion of Al-Ti-Ca complex deoxidized steel with Ce treatment. *Physica B* **558**, 10–19 (2019).
28. Liu, X., Yang, J. C., Yang, L. & Gao, X. Z. Effect of Ce on inclusions and impact property of 2Cr13 stainless steel. *J. Iron. Steel Res. Int.* **17**, 59–64 (2010).
29. Park, J. O., Suter, T. & Böhni, H. Role of manganese sulfide inclusions on pit initiation of super austenitic stainless steels. *Corrosion* **59**, 59–67 (2003).
30. Vuillemin, B. et al. SVET, AFM and AES study of pitting corrosion initiated on MnS inclusions by microinjection. *Corros. Sci.* **45**, 1143–1159 (2003).
31. Zhang, L. F. & Thomas, B. G. State of the art in evaluation and contol of steel cleanliness. *ISIJ Int* **43**, 271–291 (2003).
32. Kang, Y., Li, F., Morita, K. & Sichen, D. Mechanism study on the formation of liquid calcium aluminate inclusion from $MgAl_2O_3$ spinel. *Steel Res. Int.* **77**, 785–792 (2006).
33. Lis, T. Modification of oxygen and sulphur inclusions in steel by calcium treatment. *Metalurgija* **48**, 95–98 (2009).
34. Shao, X. J., Wang, X. H., Jiang, M., Wang, W. J. & Huang, F. X. Effect of heat treatment conditions on shape control of large-sized elongated MnS inclusions in resulfurized free-cutting steels. *ISIJ Int.* **51**, 1995–2001 (2011).
35. Yang, W. et al. Characteristics of Inclusions in low carbon Al-killed steel during ladle furnace refining and calcium treatment. *ISIJ Int.* **53**, 1401–1410 (2013).
36. Zhang, L. F. et al. Modelling of non-metallic inclusions in steel. *Miner. Process. Extr. M* **129**, 184–206 (2020).
37. Sarma, D. S., Karasev, A. V. & Jönsson, P. G. On the role of non-metallic inclusions in the nucleation of acicular ferrite steels. *ISIJ Int.* **49**, 1063–1074 (2009).
38. Ueda, S., Yamaguchi, K. & Takeda, Y. Phase equilibrium and activities of Fe-S-O melts. *Mater. Trans.* **49**, 572–578 (2008).
39. Furuseth, S. & Kjekshus, A. On the properties of α-MnS and MnS_2. *Acta Chem. Scand.* **19**, 1405–1410 (1965).
40. Juvonen, P. Effects of Non-Metallic Inclusions on Fatigue Properties of Calcium Treated Steels, (Ph.D. Academic Thesis, 2004).
41. Riedel, R. (Ed.) Handbook of Ceramic Hard Materials, 1st edn, Vol 1 (Academic, 2000).
42. Brooksbank, D. & Andrews, K. Stress field around inclusions and their relation to mechanical properties. In: Proceedings of the Production and Application of Clean Steels 186–198 (Balatonfured, Hungary, 1970).
43. Leung, C. & Vlack, L. V. Solution and precipitation hardening in (Ca, Mn) sulfides and selenides. *Metall. Mater. Trans. A* **12**, 987–991 (1981).
44. Wang, L. W. et al. Influence of inclusions on initiation of pitting corrosion and stress corrosion cracking of X70 steel in near-neutral pH environment. *Corros. Sci.* **147**, 108–127 (2019).
45. Bäßler, R. Materials Handbook—A Concise Desktop Reference, 3rd edn (Springer, 2020).
46. Oikawa, K., Ishida, K. & Nishizawa, T. Effect of titanium addition on the formation and distribution of MnS inclusions in steel during solidification. *ISIJ Int.* **37**, 332–338 (1997).
47. Yan, J., Li, T., Shang, Z. & Guo, H. Three-dimensional characterization of MnS inclusions in steel during rolling the process. *Mater. Charact.* **158**, 109944 (2019).
48. Abraham, S., Bodnar, R., Raines, J. & Wang, Y. F. Inclusion engineering and metallurgy of calcium treatment. *J. Iron. Steel Res. Int.* **25**, 133–145 (2018).
49. Baba, Y., Gao, X., Ueda, S. & Kitamura, S. Y. Sulfide capacities of solid oxides in calcium-aluminate systems. *ISIJ Int.* **60**, 1617–1623 (2020).
50. Kim, S. J., Kageyama, M., Gao, X., Ueda, S. & Kitamura, S. Y. Solubility of sulfur in the solid oxide of the calcium-aluminate system. *ISIJ Int.* **59**, 1752–1755 (2019).
51. Zhao, D. W., Li, H. B., Bao, C. L. & Yang, J. Inclusion evolution during modification of alumina inclusions by calcium in liquid steel and deformation during hot rolling process. *ISIJ Int.* **55**, 2115–2124 (2015).
52. Wang, Y. F., Cheng, G. X., Wu, W. & Li, Y. Role of inclusions in the pitting initiation of pipeline steel and the effect of electron irradiation in SEM. *Corros. Sci.* **130**, 252–260 (2018).
53. Yang, S. F., Wang, Q. Q., Zhang, L. F., Li, J. S. & Peaslee, K. Formation and modification of $MgO{\cdot}Al_2O_3$-based inclusions in alloy steels. *Metall. Mater. Trans. B* **43**, 731–750 (2012).
54. Yang, S. F., Li, J. S., Wang, Z. F., Li, J. & Lin, L. Modification of $MgO{\cdot}Al_2O_3$ spinel inclusions in Al-killed steel by Ca-treatment. *Int. J. Min. Met. Mater.* **18**, 18–23 (2011).
55. Deng, Z. Y. & Zhu, M. Y. Evolution mechanism of non-metallic inclusions in Al-killed alloyed steel during secondary refining process. *ISIJ Int.* **53**, 450–458 (2013).
56. Deng, Z. Y., Liu, Z. H., Zhu, M. Y. & Huo, L. Q. Formation, evolution and removal of $MgO{\cdot}Al_2O_3$ spinel inclusions in steel. *ISIJ Int.* **61**, 1–15 (2021).
57. Ghosh, P., Ray, R. K., Bhattacharya, B. & Bhargava, S. Precipitation and texture formation in two cold rolled and batch annealed interstitial-free high strength steels. *Scr. Mater.* **55**, 271–274 (2006).
58. Duan, H. J., Zhang, Y., Ren, Y. & Zhang, L. F. Distribution of TiN inclusions in Ti-stabilized ultra-pure ferrite stainless steel slab. *J. Iron. Steel Res. Int.* **26**, 962–972 (2018).
59. Liu, G. et al. Fast shape evolution of TiN microcrystals in combustion synthesis. *Cryst. Growth Des.* **6**, 2404–2411 (2006).
60. Shang, Z. Q., Li, T., Yang, S. F., Yan, J. C. & Guo, H. Three-dimensional characterization of typical inclusions in steel by X-ray Micro-CT. *J. Mater. Res. Technol.* **9**, 3686–3698 (2020).
61. Ooi, S. W. & Fourlaris, G. A comparative study of precipitation effects in Ti only and Ti-V ultra low carbon (ULC) strip steels. *Mater. Charact.* **56**, 214–226 (2006).
62. Beidokhti, B., Koukabi, A. H. & Dolati, A. Influences of titanium and manganese on high strength low alloy SAW weld metal properties. *Mater. Charact.* **60**, 225–233 (2009).
63. Haq, A. J., Muzaka, K., Dunne, D. P., Calka, A. & Pereloma, E. V. Effect of microstructure and composition on hydrogen permeation in X70 pipeline steels. *Int. J. Hydrog. Energy* **38**, 2544–2556 (2013).
64. Tan, J. B. et al. Role of TiN inclusion on corrosion fatigue behavior of Alloy 690 steam generator tubes in borated and lithiated high temperature water. *Corros. Sci.* **88**, 349–359 (2014).
65. Wang, Y. H. et al. Correlation between active/inactive (Ca, Mg, Al)-O_x-S_y inclusions and localised marine corrosion of EH36 steels. *J. Mater. Res. Technol.* **13**, 2419–2432 (2021).
66. Zheng, S. J. et al. Identification of $MnCr_2O_4$ nano-octahedron in catalysing pitting corrosion of austenitic stainless steels. *Acta Mater.* **58**, 5070–5085 (2010).
67. Nishimoto, M., Muto, I., Sugawara, Y. & Hara, N. Cerium addition to CaS inclusions in stainless steel: Insolubilizing water-soluble inclusions and improving pitting corrosion resistance. *Corros. Sci.* **180**, 109222 (2021).
68. Roine, A. HSC Chemistry Thermo-Chemical Database, Version 6.1, Outotec Research Oy, Pori, Finland, (2007).
69. Wei, J., Dong, J. H., Ke, W. & He, X. Y. Influence of inclusions on early corrosion development of ultra-low carbon bainitic steel in NaCl solution. *Corrosion* **71**, 1467–1470 (2014).
70. Rieders, N., Nandasiri, M., Mogk, D. & Avci, R. New insights into sulfide inclusions in 1018 carbon steels. *Metals* **11**, 428 (2021).
71. Nishimoto, M., Muto, I., Sugawara, Y. & Hara, N. Artificial MnS inclusions in stainless steel: Fabrication by spark plasma sintering and corrosion evaluation by microelectrochemical measurements. *ISIJ Int.* **60**, 196–198 (2020).
72. Nishimoto, M., Muto, I., Sugawara, Y. & Hara, N. Morphological characteristics of trenching around MnS inclusions in type 316 stainless steel: The role of molybdenum in pitting corrosion resistance. *J. Electrochem. Soc.* **166**, C3081–C3089 (2019).
73. Shi, W., Yang, S., Dong, A. & Li, J. Understanding the corrosion mechanism of spring steel induced by MnS inclusions with different sizes. *Jom* **70**, 2513–2522 (2018).
74. Man, C., Dong, C. F., Xiao, K., Yu, Q. & Li, X. G. The Combined effect of chemical and structural factors on pitting corrosion induced by MnS-(Cr, Mn, Al) O duplex inclusions. *Corrosion* **74**, 312–325 (2017).
75. Chao, Q. et al. On the enhanced corrosion resistance of a selective laser melted austenitic stainless steel. *Scr. Mater.* **141**, 94–98 (2017).
76. Chiba, A., Muto, I., Sugawara, Y. & Hara, N. Effect of atmospheric aging on dissolution of MnS inclusions and pitting initiation process in type 304 stainless steel. *Corros. Sci.* **106**, 25–34 (2016).
77. Torkkeli, J., Saukkonen, T. & Hänninen, H. Effect of MnS inclusion dissolution on carbon steel stress corrosion cracking in fuel-grade ethanol. *Corros. Sci.* **96**, 14–22 (2015).
78. Krawiec, H., Vignal, V. & Oltra, R. Use of the electrochemical microcell technique and the SVET for monitoring pitting corrosion at MnS inclusions. *Electrochem. Commun.* **6**, 655–660 (2004).
79. Chiba, A., Muto, I., Sugawara, Y. & Hara, N. Pit initiation mechanism at MnS inclusions in stainless steel synergistic effect of elemental sulfur and chloride ions. *J. Electrochem. Soc.* **160**, C511–C520 (2013).
80. Zhou, Y. T., Zheng, S. J., Zhang, B. & Ma, X. L. Atomic scale understanding of the interaction between alloying copper and MnS inclusions in stainless steels in NaCl electrolyte. *Corros. Sci.* **111**, 414–421 (2016).
81. Kovalov, D., Taylor, C. D., Heinrich, H. & Kelly, R. G. Operando electrochemical TEM, ex-situ SEM and atomistic modeling studies of MnS dissolution and its role in triggering pitting corrosion in 304L stainless steel. *Corros. Sci.* **199**, 110184 (2022).

82. Deva, A., De, S. K. & Jha, B. K. Effect of B/N ratio on plastic anisotropy behaviour in low carbon aluminium killed steel. *Mater. Sci. Technol.* **24**, 124–126 (2013).
83. Deng, X. et al. Inclusion behaviour in aluminium-killed steel during continuous casting. *Ironmak. Steelmak.* **46**, 522–528 (2018).
84. Li, G. X. et al. Dissolution kinetics of the sulfide-oxide complex inclusion and resulting localized corrosion mechanism of X70 steel in deaerated acidic environment. *Corros. Sci.* **174**, 108815 (2020).
85. Tyurin, A. G., Pyshmintsev, I. Y., Kostitsyna, I. V. & Zubkova, I. M. Thermodynamics of chemical and electrochemical stability of corrosion active nonmetal inclusions. *Prot. Met.* **43**, 34–44 (2007).
86. Reformatskaya, I. I. & Freiman, L. I. Precipitation of sulfide inclusions in steel structure and their effect on local corrosion processes. *Prot. Met. Phys. Chem.* **37**, 511–516 (2001).
87. Chen, H., Lu, L., Huang, Y. H. & Li, X. G. Insight into TiN inclusion induced pit corrosion of interstitial free steel exposed to aerated NaCl solution. *J. Mater. Res. Technol.* **13**, 13–24 (2021).
88. Iannuzzi, M., Vasanth, K. L. & Frankel, G. S. Unusual correlation between SKPFM and corrosion of nickel aluminum bronzes. *J. Electrochem. Soc.* **164**, C488–C497 (2017).
89. Huang, H., Wang, H., Zhang, J. & Yan, D. Surface potential images of polycrystalline organic semiconductors obtained by Kelvin probe force microscopy. *Appl. Phys. A* **95**, 125–130 (2009).
90. Liu, P., Zhang, Q. H., Li, X. R., Hu, J. M. & Cao, F. H. Insight into the triggering effect of (Al, Mg, Ca, Mn)-oxy-sulfide inclusions on localized corrosion of weathering steel. *J. Mater. Sci. Technol.* **64**, 99–113 (2021).
91. Avasarala, B. & Haldar, P. Electrochemical oxidation behavior of titanium nitride based electrocatalysts under PEM fuel cell conditions. *Electrochim. Acta* **55**, 9024–9034 (2010).
92. Harrington, S. P. & Devine, T. M. The influence of the semiconducting properties of passive films on localized corrosion rates. *ECS Trans.* **16**, 117–123 (2009).
93. Munirathinam, B., Narayanan, R. & Neelakantan, L. Electrochemical and semiconducting properties of thin passive film formed on titanium in chloride medium at various pH conditions. *Thin Solid Films* **598**, 260–270 (2016).
94. Zhang, S., Liu, J., Tang, M., Zhang, X. & Wu, K. M. Role of rare earth elements on the improvement of corrosion resistance of micro-alloyed steels in 3.5 wt.% NaCl solution. *J. Mater. Res. Technol.* **11**, 519–534 (2021).
95. Wei, W. Z. et al. In-situ characterization of initial marine corrosion induced by rare-earth elements modified inclusions in Zr-Ti deoxidized low-alloy steels. *J. Mater. Res. Technol.* **9**, 1412–1424 (2020).
96. Zhang, X. et al. Effects of niobium and rare earth elements on microstructure and initial marine corrosion behavior of low-alloy steels. *Appl. Surf. Sci.* **475**, 83–93 (2019).
97. Tang, M. et al. Mechanism understanding of the role of rare earth inclusions in the initial marine corrosion process of microalloyed steels. *Materials* **12**, 1–15 (2019).
98. Liu, Z. et al. Effects of rare earth elements on corrosion behaviors of low-carbon steels and weathering steels. *Mater. Corros.* **71**, 258–266 (2019).
99. Kim, S. T., Jeon, S. H., Lee, I. S. & Park, Y. S. Effects of rare earth metals addition on the resistance to pitting corrosion of super duplex stainless steel-Part 1. *Corros. Sci.* **52**, 1897–1904 (2010).
100. Zhang, B. & Ma, X. L. A review-Pitting corrosion initiation investigated by TEM. *J. Mater. Sci. Technol.* **35**, 1455–1465 (2019).
101. Shi, W. N., Yang, S. F. & Li, J. S. Effect of nonmetallic inclusions on localized corrosion of spring steel. *Int. J. Min. Met. Mater.* **28**, 390–397 (2021).
102. Li, W., Li, J. Y., Gu, J. B. & Zhang, Q. R. Correlation between hyperfine structure of inclusion and localized corrosion mechanism of DSS2101 with Ce microalloying in simulated marine environment. *Vacuum* **191**, 110361 (2021).
103. Gateman, S. M. et al. The role of titanium in the initiation of localized corrosion of stainless steel 444. *npj Mater. Degrad.* **2**, 1–8 (2018).

ACKNOWLEDGEMENTS

This work was supported by National Natural Science Foundation of China (No. 52071347), National Key Research and Development Program of China (No. 2017YFB0702302) and the National Materials Corrosion and Protection Data Center.

AUTHOR CONTRIBUTIONS

P.L. conducted the literature investigation and composed the draft manuscript with help from Q.H.Z., Y.W., T.S., and F.H.C. All authors provided revision approved the manuscript in its current form.

COMPETING INTERESTS

The authors declare no competing interests.

ADDITIONAL INFORMATION

Correspondence and requests for materials should be addressed to Fa-He Cao.

Reprints and permission information is available at http://www.nature.com/reprints

Publisher's note Springer Nature remains neutral with regard to jurisdictional claims in published maps and institutional affiliations.